
This is an electronic reprint of the original article.
This reprint may differ from the original in pagination and typographic detail.

Liu, Wenqi; Lian, Junhe; Aravas, Nikolaos; Münstermann, Sebastian

A strategy for synthetic microstructure generation and crystal plasticity parameter calibration of fine-grain-structured dual-phase steel

Published in:
INTERNATIONAL JOURNAL OF PLASTICITY

DOI:
[10.1016/j.ijplas.2019.10.002](https://doi.org/10.1016/j.ijplas.2019.10.002)

Published: 01/03/2020

Document Version
Peer reviewed version

Published under the following license:
CC BY-NC-ND

Please cite the original version:
Liu, W., Lian, J., Aravas, N., & Münstermann, S. (2020). A strategy for synthetic microstructure generation and crystal plasticity parameter calibration of fine-grain-structured dual-phase steel. *INTERNATIONAL JOURNAL OF PLASTICITY*, 126, [102614]. <https://doi.org/10.1016/j.ijplas.2019.10.002>

Journal Pre-proof

A strategy for synthetic microstructure generation and crystal plasticity parameter calibration of fine-grain-structured dual-phase steel

Wenqi Liu, Junhe Lian, Nikolaos Aravas, Sebastian Münstermann



PII: S0749-6419(19)30372-9

DOI: <https://doi.org/10.1016/j.ijplas.2019.10.002>

Reference: INTPLA 2614

To appear in: *International Journal of Plasticity*

Received Date: 1 June 2019

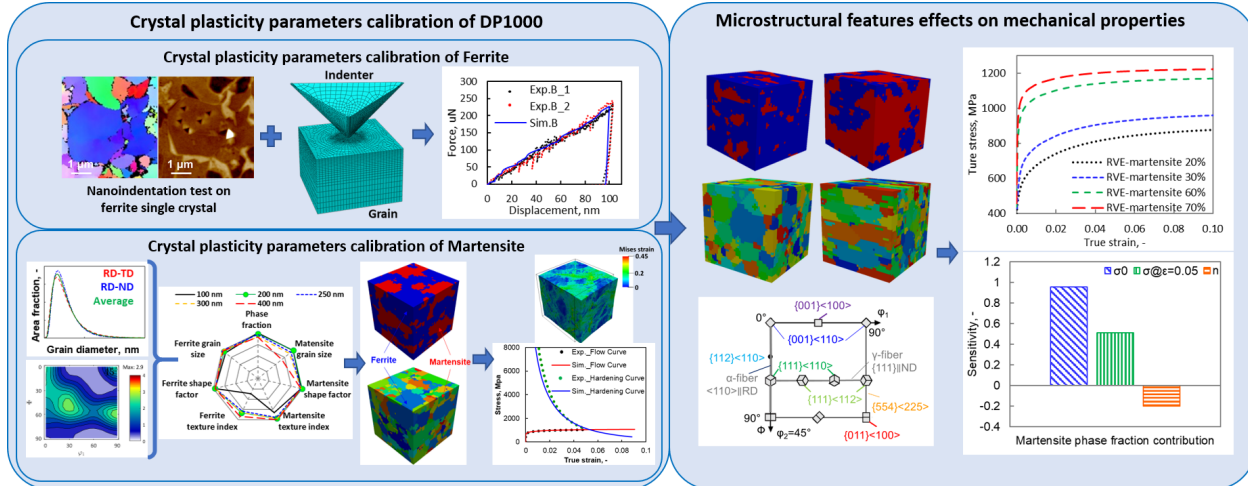
Revised Date: 22 September 2019

Accepted Date: 4 October 2019

Please cite this article as: Liu, W., Lian, J., Aravas, N., Münstermann, S., A strategy for synthetic microstructure generation and crystal plasticity parameter calibration of fine-grain-structured dual-phase steel, *International Journal of Plasticity*, <https://doi.org/10.1016/j.ijplas.2019.10.002>.

This is a PDF file of an article that has undergone enhancements after acceptance, such as the addition of a cover page and metadata, and formatting for readability, but it is not yet the definitive version of record. This version will undergo additional copyediting, typesetting and review before it is published in its final form, but we are providing this version to give early visibility of the article. Please note that, during the production process, errors may be discovered which could affect the content, and all legal disclaimers that apply to the journal pertain.

© 2019 Elsevier Ltd. All rights reserved.



A strategy for synthetic microstructure generation and crystal plasticity parameter calibration of fine-grain-structured dual-phase steel

Wenqi Liu¹, Junhe Lian^{2,3*}, Nikolaos Aravas^{4,5}, Sebastian Münstermann¹

¹Integrity of Materials and Structures, Steel Institute, RWTH Aachen University, Intzestraße 1, 52072 Aachen, Germany

²Advanced Manufacturing and Materials, Department of Mechanical Engineering, Aalto University, Puumiehenkuja 3, 02150 Espoo, Finland

³Impact and Crashworthiness Lab, Department of Mechanical Engineering, Massachusetts Institute of Technology, 77 Massachusetts Avenue, Cambridge, MA 02139-4307, USA

⁴Department of Mechanical Engineering, University of Thessaly, Volos 38334, Greece

⁵International Institute for Carbon Neutral Energy Research (WPI-I2CNER), Kyushu University, 744 Moto-oka, Nishi-ku, Fukuoka 819-0395, Japan

* Corresponding author.

E-mail address: junhe.lian@aalto.fi; lianjh@mit.edu

Phone: +358 50 477 0765

Abstract

This study aims to establish a strategy for bridging the microstructure and mechanical properties of fine-grain-structured dual-phase steel. A complete workflow is built up commencing with the microstructure observations and characterization in both phase and grain levels by assorted experimental techniques. An assessment criterion is proposed to quantitatively examine the representativeness of synthetic microstructure models in terms of the refined microstructural features including phase fraction, grain size, grain shape, and texture for each phase of the steel. The criterion is employed to define a two-step optimization procedure for building the synthetic microstructure model for the DP steel with nanoscale grain size. The crystal plasticity model is employed to describe the material deformation behavior. The corresponding material parameters are calibrated by an inverse approach combining the micromechanical nanoindentation test and the macroscopic uniaxial tensile test. The simulation with the calibrated parameters and the synthetic microstructure model gives an excellent prediction of the Lankford coefficient of the dual-phase steel. Benefiting from the strategy, a virtual laboratory is conducted to investigate the microstructure sensitivity on the mechanical properties, which serves a basis for the microstructure design with desired properties.

Keywords

Micromechanical modeling, Dual-phase steel, Microstructure, Representative volume element, Crystal plasticity; DP1000

1 Introduction

It is well known that the properties of metallic materials are affected by all microstructural features including the spatial distribution of phases, grains, inclusions, and even defects (Gottstein, 2004). For instance, the conventional dual-phase (DP) steels with a microstructure of ferrite matrix and dispersive martensite (normally 5-30%) show the low yielding strength around 300-380 MPa and the ultimate tensile strength within 600-700 MPa (Fonstein, 2017; Golovanenko and Fonstein, 1986), whereas the recently developed DP steels with higher martensite phase fraction up to 50-70% enhance the tensile strength to 800-1200 MPa (Horvath, 2010). In addition to the phase fraction, the microstructural features in grain level for both phases, such as the distribution of grain size, shape, and crystallographic orientation are considered as the key factors that affect the macroscopic mechanical properties and the structural performances of the steels (Avramovic-Cingara et al., 2009; Bag et al., 1999; Kadkhodapour et al., 2011; Kang et al., 2007; Lai et al., 2016; Pierman et al., 2014; Schmitz and Prahl, 2016; Shen et al., 1986; Tasan et al., 2015; Tasan et al., 2014).

Recently, various numerical approaches were developed under the frame of the integrated computational materials and engineering (ICME) to offer the qualitative and/or quantitative description for the microstructure-property relationship coupling multiscale material models and microstructure models, such as molecular dynamics (MD) or Monte Carlo (MC) method for the descriptions of the inherent properties at the atomistic level (Fermi et al., 1955; Prieto-Depedro et al., 2015; Shinzato et al., 2019; Xu et al., 2013), dislocation dynamics (DD) for modelling of the dislocation motions at mesoscale (Akarapu et al., 2010; Fivel, 2010; Jiang et al., 2019), and crystal plasticity (CP) for the crystal and phase level mechanical properties predication (Roters et al., 2010; Zhang et al., 2016), as well as the representative volume element (RVE), statistical volume element (SVE), or uncorrelated volume element (UVE) for the microstructure descriptions (Hill, 1963; Madivala et al., 2018; Sanei and Fertig, 2015; Yin et al., 2008). Among these approaches, considering the length scale applicability and calculation efficiency for solving engineering problems, the CP models in combination with RVEs (Diehl et al., 2017a; Uthaisangsuk et al.,

2011; Vajragupta et al., 2014) have attracted great attention in the material and mechanical engineering fields.

The crystal plasticity theory based on dislocation motion on slip systems was firstly proposed by Taylor (Taylor, 1934a, b). In early-stage numerical approaches, the continuum constitutive equations were proposed (Hill, 1966; Hill and Rice, 1972; Rice, 1971) and utilized to calculate the dislocation-slip-accumulated strain and predict the macrotexture evolution (Becker, 1991; Eisenlohr and Roters, 2008). The constitutive laws can be divided into two groups: phenomenological laws considering the critical stress as the state variable for dislocation motion while the physical-based laws taking into account the material physical features such as dislocation density. Except for dislocation slip, twinning (Hama and Takuda, 2011), phase transformation (Ma and Hartmaier, 2015), or other micromechanical deformation mechanisms are also investigated by CP models. Successful applications of the CP model can be found in the prediction of ears during cupping (Raabe and Roters, 2004; Zhao et al., 2004), the anisotropic deformation behavior (Kraska et al., 2009; Van Houtte et al., 2006; Xie et al., 2018d), yield locus and hardening curves (Lian et al., 2017; Zhang et al., 2016), strain gradient effects (Arsenlis et al., 2004; Arsenlis and Parks, 1999; Arsenlis and Parks, 2002; Ma et al., 2006a, b, c), residual stress formation during deformation (Xie et al., 2018a; Xie et al., 2018b), and the correlation to damage and fatigue (Diehl et al., 2017b; Gu et al., 2019; McDowell and Dunne, 2010; Prasannavenkatesan et al., 2011; Xie et al., 2018c).

Problem definition

Despite this successful development and application of the CP model, one could notice that they are mainly focused on single-phase materials. For the DP or multiphase steels, the existing results are mainly qualitative. Two open questions for the limitation identified by the present study are i) calibration of reliable crystal plasticity parameters for every single phase of the multiphase materials and ii) the establishment of meaningful synthetic microstructure. The difficulty increases when the material features a micro or nanoscale grain structure.

Parameter calibration of CP models

In current literature, the force–displacement or stress–strain response obtained from macroscopic tests, e.g. uniaxial tensile tests (Zhang et al., 2015), fatigue tests (Yu et al., 2015) and the combination of multiple tests (Ebeling et al., 2009), or micromechanical tests, such as nanoindentation (Zambaldi et al., 2012) and pillar tests (Soler et al., 2012; Zheng et al., 2018) are generally employed for CP parameter calibration. Most of these approaches only gain success in single-phase materials; however, it is greatly challenged by the advanced high-strength steels (AHSS), where DP or multi-phase structures are found, and each phase contains very fine grains. The macroscopic mechanical tests alone are simply not suitable anymore to fit the CP parameters for more than one phase. The very fine grains, even ferrites for some cases with the average grain size of 2-3 microns, on the one hand, brings difficulties in characterizing the mechanical behavior of single crystals locally and on the other hand the fine hierarchical structure, e.g. martensite raises up great uncertainty in the micromechanical tests.

In existing literature, the CP parameters of martensite phase in DP steel is either directly taken from a single-phase martensite with similar chemical composition (Tasan et al., 2014), or the parameter determination is based on the empirical equations from chemical compositions (Bong et al., 2017), which both lack a certain level of confidence in the specific material and application. Another approach combining the macroscopic stress–strain response and lattice strains of individual ferrite and martensite phase measured by an in situ neutron diffraction experiment under uniaxial tension was also developed to identify the parameters of each phase (Choi et al., 2013; Kim et al., 2017; Ravi et al., 2019; Woo et al., 2012). However, despite the limited access to the equipment for the lattice strain measurement, the quality of this technique is distinctly affected by the identification of the lattice strain of ferrite and martensite due to their similar crystal structures.

Synthetic microstructure model for DP steels

In terms of microstructure model generation, various types of RVEs were developed for polycrystal metals. The first straightforward RVE generation approach is the digitization of the real microstructure (Choi et al., 2013; Lian et al., 2014; Raabe et al., 2001), which is straightforward but also shows the obvious drawbacks in keeping the statistical representativeness of the microstructure and manipulating the

microstructure configurations in the microstructure design phase. Hence, for materials with complex and statistically homogenous microstructure, a synthetic RVE containing sufficient microstructural information should be a satisfactory tool. For this type of RVEs, some simple approaches create a regular cube RVE with the voxel mesh for uniform cube grains, in which only crystal orientations can be introduced (Mahnken et al., 2015; Raabe et al., 2002a; Raabe et al., 2002b; Woo et al., 2012). Regarding more complex morphology description, different Voronoi tessellation algorithms are intensively developed and applied considering the phase and grain patterns (Quey et al., 2011; Teferra and Graham-Brady, 2015) and the hierarchical martensitic steel (Li et al., 2018) and bainitic steel (Osipov et al., 2008). Recent advance on the synthetic RVEs focuses on representing more microstructural features including phase fraction, grain size, grain shape, neighboring grain number, and grain orientation (Ghosh et al., 2016; Groeber and Jackson, 2014). Generally, most algorithms show satisfactory performance on the phase and grain configurations such as average size and shape and give fair results on corresponding grain size and shape distribution functions. However, for DP or multi-phase materials, these grain-level characteristics are rarely compared with the experimental measurement. In addition, the grain crystallographic orientation shall be properly and separately studied in the RVE due to the possibly very distinct texture of different phases. Instead, a typical assumption used in most current RVEs is the random texture for all phases. The reasons are mainly two folds: i) a general and accurate algorithm for generating multi-phase synthetic RVEs with statistical distribution information for grain size, shape, and crystallographic orientation is not well established; and ii) a quantitative evaluation criterion of the representativeness of RVEs to the experimental characterization is missing.

For single-phase materials, a semi-quantitative proposal is mainly employed, that an adequate number of grains, typically a few hundred, shall be included in the RVE (Ghosh et al., 2016); however, this method will not be suitable for a heterogeneous DP or multi-phase structure, where different phases have very distinct grain sizes. The reason is simply that the mesh size of the RVE is defined by the very fine grains and to ensure a certain number of grains with large grains size may result in elements with a magnitude of 10^9 , which will significantly challenge the computational time and memory size for even modern

computer workstations. Accordingly, a tool to measure the quality of the representativeness of RVE is desired, as it will enable more flexible design of the RVE without the semi-quantitative restrictions in the existing studies (Ghosh et al., 2016; Mandal et al., 2018; Nakamachi et al., 2007), such as grain number. Automatically, it will result in an optimized synthetic RVE that is able to represent the phase fraction and the statistical distribution of grains size, shape, and texture at the same time.

Aim and scope of the current study

Viewing the scientific gaps presented by the literature review, it is clearly concluded that lacking proper solutions for the two questions identified by the presenting authors, i) construction of meaningful and representative synthetic microstructure and ii) parameter calibration of every individual phase, is significantly hindering the application of the micromechanical modeling approach with CP model for dual-phase steels for predictive and quantitative analysis. Therefore, the present study aims to provide solutions for these two open questions by proposing a microstructure representativeness assessment criterion and a parameter calibration procedure of the crystal plasticity model for the fine-grain-structured dual-phase steels. The application of such a criterion will improve significantly the accuracy and efficiency in building the structure-property relation and material design using computational methods and a trustworthy and effective approach to calibrate CP parameters for complex fine-grain DP microstructures will provide more confidence in the application of the strategy for quantitative analysis. In this study, the details of constructing the strategy will be shown and its predictive capability will be shown by analyzing the stress and r-value anisotropy for a high-strength DP1000 steel.

The workflow starts from the microstructure characterization by light optical microscopy (LOM), scanning electron microscopy (SEM) and electron backscatter diffraction (EBSD) techniques in section 2. In terms of the material model, the constitutive equations in the CP model are formulated in section 3. Then, section 4 explains the proposed quantitative assessment criterion for RVE representativeness and its application to determine the optimal RVE for the reference material. Section 5 presents the material parameters calibration approach coupling the macroscopic uniaxial tensile tests and the microscopic nanoindentation tests. Consequently, a virtual laboratory is built up in section 6 to demonstrate the

application of the strategy as well as draw conclusions of the microstructure effects on the plastic flow properties.

2 Material characterization

The investigated material in this study is a DP1000 steel sheet with a thickness of 1.5 mm. Various investigation techniques and analysis software are employed for the microstructure analysis. In addition, to get more accurate microstructure information for 3D RVE modeling, the rolling direction – transverse direction (RD-TD) plane as well as the rolling direction – normal direction (RD-ND) plane are investigated. Generally, the microstructure characterization for a DP structure includes three parts: inclusions analysis, phase analysis, and grain-level analysis.

According to the LOM examination in Fig. 1, the DP1000 is composed of ferrite and martensite. After etching, the ferrite phase shows a brighter area while the martensite phase is grey and dark. The main inclusion is the TiN particle with a fraction of 0.05%, which will not be considered in the RVEs. Due to the fine microstructure, the LOM technique is failing to offer accurate phase identification. Accordingly, SEM is employed and to obtain a statistically representative description of the martensite phase fraction, eight spots are randomly chosen on an upper RD-TD plane (0.1 mm down from the material original top surface to remove manufacturing influence during sample preparation) with variable magnification from 1000X to 10000X. In addition, eight positions are also measured along the whole thickness direction on the RD-ND plane. Fig. 2 sketches the measurement positions and illustrates three SEM graphs from these 16 positions.

Furthermore, the grain-level material microstructure information, such as grain size, shape, misorientation, and orientation, are gained by the EBSD method. The investigated surface is prepared with mechanical grinding and then electropolishing to remove the surface deformation and residual stress. The total investigated dimension is $100 \mu\text{m} \times 100 \mu\text{m}$ on each plane. Fig. 3 displays partial EBSD orientation maps on both RD-TD and RD-ND planes with a dimension of $50 \mu\text{m} \times 50 \mu\text{m}$. The measurement step size is 50 nm due to the fine grain structure of the investigated material. The detailed analysis of microstructure features is introduced in section 4.1.

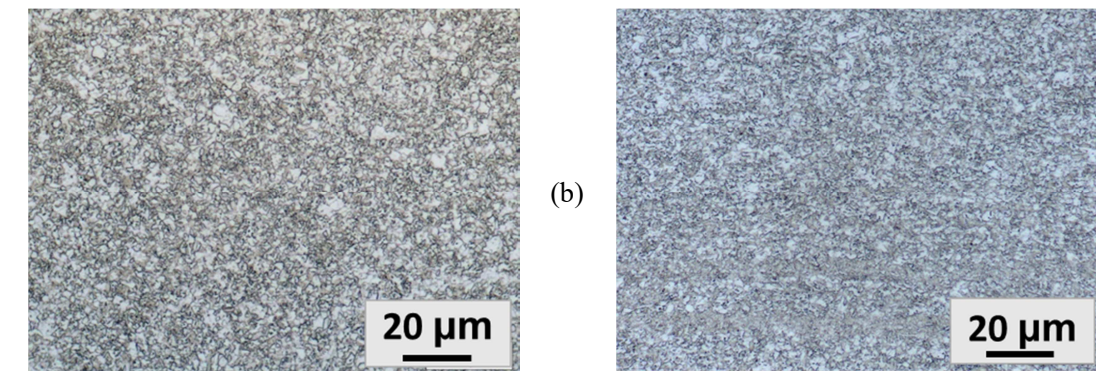


Fig. 1 LOM metallographs of DP1000 on (a) RD-TD and (b) RD-ND planes.

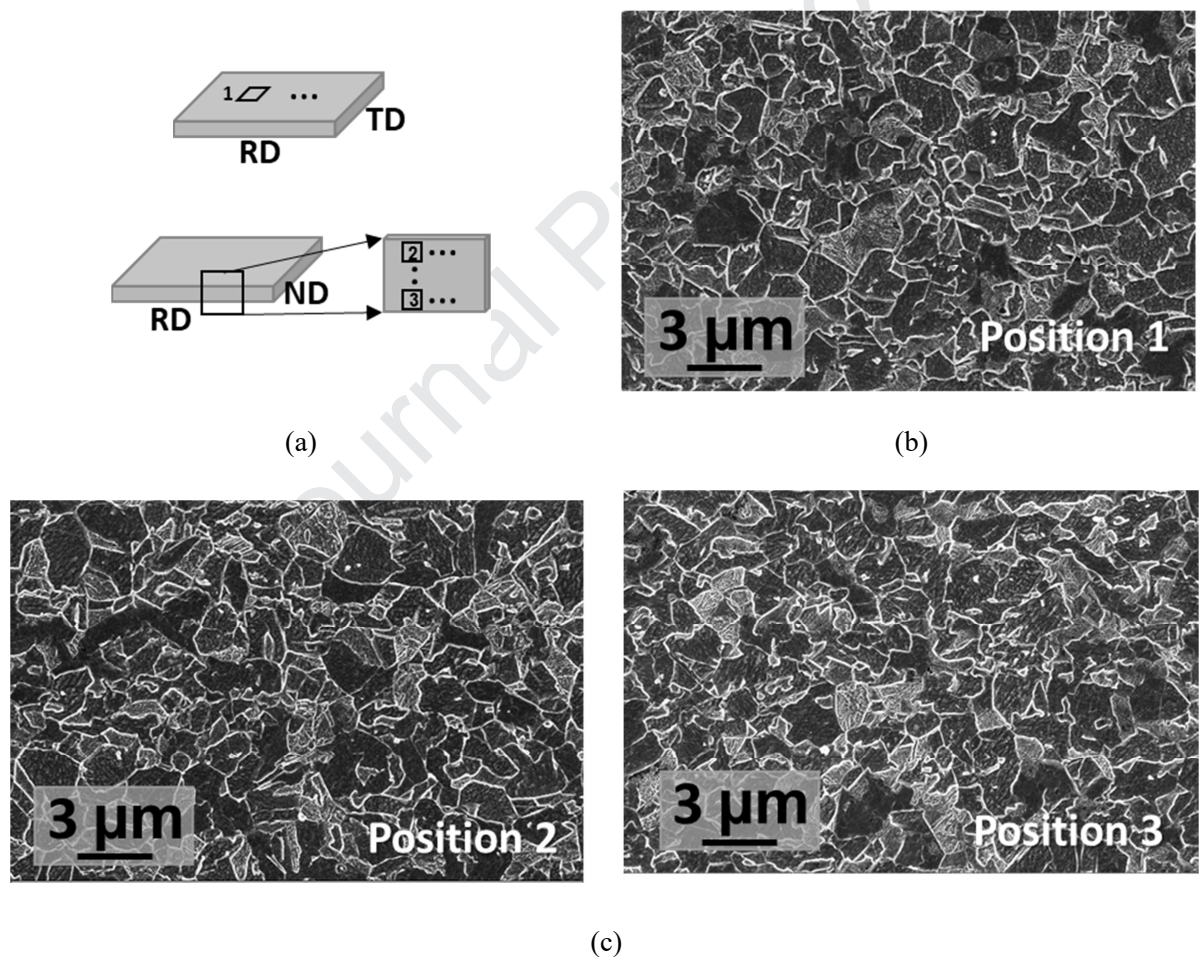


Fig. 2 SEM measurement plan (a) and the metallographs of DP1000 on RD-TD (b) and RD-ND (c) planes.

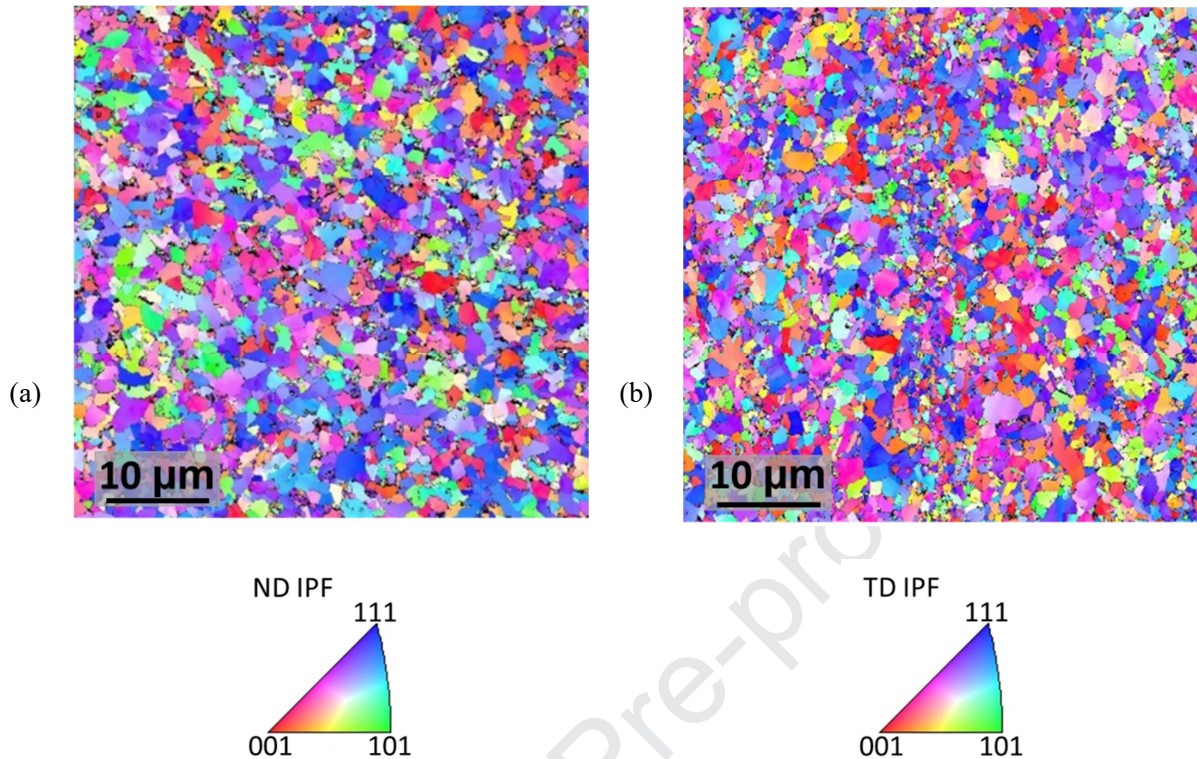


Fig. 3 EBSD orientation maps of DP1000 on (a) RD-TD and (b) RD-ND planes.

3 Constitutive model

The crystal plasticity modeling formulation based on dislocation slip is used in this study. The governing equations of the model (Roters et al., 2010) are briefly introduced in the following.

The deformation gradient \mathbf{F} is multiplicatively decomposed into a purely elastic (reversible) part \mathbf{F}_e and a purely plastic (irreversible) part \mathbf{F}_p (Asaro and Lubarda, 2006):

$$\mathbf{F} = \mathbf{F}_e \mathbf{F}_p \quad \text{Eq. 1}$$

where \mathbf{F}_p is the deformation solely due to plastic shearing on crystallographic slip systems and \mathbf{F}_e results from the stretching and rotation of the crystal lattice. The deformation in Eq. 1 can be envisioned as accomplished in two stages: material first moves through the undeformed crystal lattice according to \mathbf{F}_p and then the lattice and material deform together giving rise to \mathbf{F}_e .

The derivation of the plastic deformation gradient rate $\dot{\mathbf{F}}_p$ is expressed as:

$$\dot{\mathbf{F}}_p = \mathbf{L}_p \mathbf{F}_p \quad \text{Eq. 2}$$

where \mathbf{L}_p is the plastic velocity gradient. If the deformation process involves only dislocation slip, \mathbf{L}_p is defined as:

$$\mathbf{L}_p = \sum_{\alpha=1}^N \dot{\gamma}^\alpha \mathbf{m}^\alpha \otimes \mathbf{n}^\alpha \quad \text{Eq. 3}$$

where for slip system α , \mathbf{m}^α and \mathbf{n}^α are the unit vector describing the slip direction and normal direction to the slip plane; $\dot{\gamma}^\alpha$ is the slip rate and N is the number of active slip systems. The shear rate $\dot{\gamma}^\alpha$ is determined by the resolved shear stress τ^a and the critical resolved shear stress τ_c^a . The kinetic law on the slip system α is defined as:

$$\dot{\gamma}^\alpha = \dot{\gamma}_0 \left| \frac{\tau^a}{\tau_c^a} \right|^m \operatorname{sgn}(\tau^a) \quad \text{Eq. 4}$$

where $\dot{\gamma}_0$ and m are the reference shear rate and rate sensitivity of slip system α respectively. The resolved shear stress τ^a on slip system α is defined as:

$$\tau^a = \mathbf{S} \cdot (\mathbf{m}^\alpha \otimes \mathbf{n}^\alpha) \quad \text{Eq. 5}$$

where \mathbf{S} is the second Piola-Kirchhoff stress in the intermediate configuration defined by \mathbf{F}_e . The micromechanical interaction between different slip systems should also be taken into consideration by:

$$\dot{\tau}_c^\alpha = \sum_{\beta=1}^N h_{\alpha\beta} |\dot{\gamma}^\beta| \quad \text{Eq. 6}$$

where $h_{\alpha\beta}$ is the hardening matrix and given as:

$$h_{\alpha\beta} = q_{\alpha\beta} \left[h_0 \left(1 - \frac{\tau_c^\beta}{\tau_c^s} \right)^a \right] \quad \text{Eq. 7}$$

where h_0 , a , and τ_c^s are slip hardening parameters. The value $q_{\alpha\beta}$ incorporates the effect of self-hardening ($\alpha = \beta$) and latent hardening ($\alpha \neq \beta$) and is assigned as 1.0 for coplanar slip and 1.4 otherwise. Therefore, the hardening evolution law of slip system α is determined according to:

$$\tau_c^\alpha = \tau_0 + \int_0^t q_{\alpha\beta} \left[h_0 \left(1 - \frac{\tau_c^\beta}{\tau_c^s} \right)^a \right] |\dot{\gamma}^\beta| dt \quad \text{Eq. 8}$$

where τ_0 is the initial critical resolved shear stress. To sum up, the involved parameters in crystal plasticity model are τ_0 , τ_c^s , h_0 , a , $\dot{\gamma}_0$ and m . Regarding the quasi-static loading condition, the strain rate effect is currently not considered in this study. Hence, the strain rate related parameters $\dot{\gamma}_0$ and m are chosen from literature (Tasan et al., 2014), as shown in Table 4. The remaining four hardening parameters for DP1000 need to be calibrated by the proposed inversely calibration strategy in the following sections.

In terms of the solution of the constitutive equations on material points, finite element method (FEM) with Gaussian integration points or fast Fourier transformation (FFT) approaches with regular Fourier points can be employed. The detailed explanations of these schemes and their implementations with CP models as well as the comparisons between these two methods have been investigated in many studies (Liu et al., 2010; Prakash and Lebensohn, 2009). Generally, the CPFFT method is an efficient replacement of the CPFEM with periodic boundary conditions due to its higher numerical performances with the economical computing time and better predictive capabilities as a mesh-free method. However, with respect to complex boundary conditions, the CPFEM method is preferred. Therefore, In this study, CPFEM is

employed for nanoindentation simulation while RVE calculations are carried out by CPFFT. The detailed information will be introduced in section 5.

4 Synthetic microstructure generation

4.1 Microstructure feature analysis

4.1.1 Phase fraction

In DP steels, as the body-centered cubic (bcc) ferrite and body-centered tetragonal (bct) martensite grains have similar crystal structures, it is not straightforward to distinguish these two phases by EBSD. Generally, martensite is characterized by lower image quality (IQ) values and larger kernel average misorientation (KAM) values due to its hierarchical microstructure compared with ferrite. Hence, a specific grain average image quality (GavgIQ) value is normally employed to distinguish martensite and ferrite in the literature (Calcagnotto et al., 2011; Tasan et al., 2015). However, this single GavgIQ criterion is not satisfied to strictly delimit two phases in some DP steels, especially for a DP1000 with fine microstructure, since some ferrite and martensite grains show similar microstructural signals, i.e. GavgIQ or KAM values. As indicated in Fig. 4, although two peaks can be observed in the GavgIQ distribution figures roughly, in contrast to most DP600 or DP800 steels, the borderline between two phases is not clear, especially for the RD-ND plane. More specifically, in the range from 115000 to 135000, the GavgIQ values of some martensite and ferrite grains are close to each other. Hence, the EBSD method cannot be used to determine the phase fraction of DP1000. Instead, the high-magnification SEM images (Fig. 2) are employed. The relatively white grain areas with irregular lath structure are regarded as martensite whereas the homogeneously dark and grey grain areas are treated as ferrite. The software Digimizer is employed to account for the phase fraction. For the statistical analysis, the average phase fraction is calculated from all inspected positions on both RD-TD and RD-ND planes. It is concluded that the investigated DP1000 has 55% ferrite and 45% martensite.

For the detailed grain-level microstructure feature analysis for individual phases, ferrite and martensite need to be separated based on the EBSD measurement. Therefore, the following procedure is proposed to separate the two phases. Firstly, 5° is used as the minimum misorientation between two neighboring measured points to reconstruct the grain boundaries, and for martensite, the blocks are generally regarded as martensite grains. Regarding the phase identification, even the GavgIQ of 12500 can give the same

phase fraction result as obtained by SEM, the uncertainty that martensite and ferrite grains still mix with each other cannot be avoided. To obtain the precise statistical microstructure information used for RVE generation, the determination of martensite and ferrite should be deliberate. Therefore, with a careful check on grain IQ maps, two IQ thresholds are chosen for two phases: $G_{avgIQ} < 115000$ for martensite grains and $G_{avgIQ} > 135000$ for ferrite grains, in order to make sure that the picked grains are definite for the phase that they belong to. The grains in the middle range, i.e. $115000 < G_{avgIQ} < 135000$ are omitted for the statistical microstructure characterization on grain level. After grain reconstruction and reselection, a workflow for the grain size, shape, misorientation, orientation distributions analysis is built up with the help of MATLAB/MTEX Toolbox (Bachmann et al., 2010; Hielscher and Schaeben, 2008; Mainprice et al., 2011).

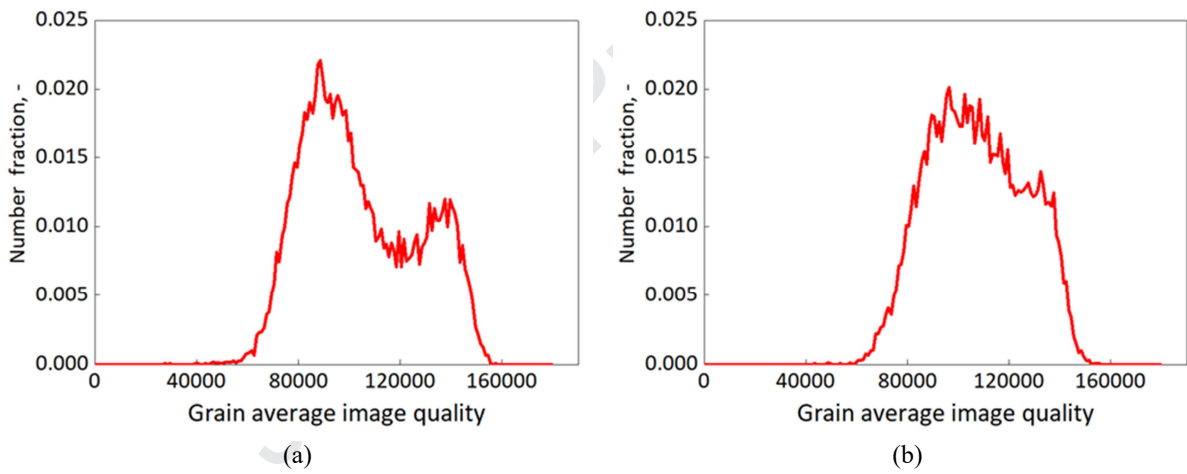


Fig. 4 Grain average image quality distribution of DP1000 on (a) RD-TD and (b) RD-ND planes.

4.1.2 Grain size distribution

The grain size distribution function is defined as the statistical frequency of specific grain size. Actually, a mathematically exact given grain size may not exist, so in general, the frequency of grains with sizes within a predefined size interval is counted and this is usually represented as a histogram (Gottstein, 2004). The grain size can be characterized by the equivalent diameter d , which is in 2D the diameter of a circle that gives the same area as the grain, or in 3D a sphere that gives the same volume as the grain. The grain size distribution of crystalline solids mostly matches the logarithmic normal distribution, i.e. the frequency

against the logarithm of the grain size ($\ln d$) follows the normal distribution tendency. In mathematics, the normal distribution of x can be represented as:

$$f(x; \mu, \sigma) = \frac{1}{\sigma\sqrt{2\pi}} \exp\left(-\frac{(x - \mu)^2}{2\sigma^2}\right) \quad \text{Eq. 9}$$

then $y = \exp(x)$ has a log-normal distribution:

$$f(y; \mu, \sigma) = \frac{1}{y\sigma\sqrt{2\pi}} \exp\left(-\frac{(\ln y - \mu)^2}{2\sigma^2}\right), \quad y > 0 \quad \text{Eq. 10}$$

where f is the probability density function; μ and σ are the mean values and standard deviation, respectively. For grain size distribution, $y = d$ and $x = \ln d$. Besides, the characterized parameters of a distribution, the mode, median, and mean values are the same in an ideal normal distribution, i.e. they are all equal to μ . However, these three values are different from each other in a log-normal distribution. The mode value is the point of the global maximum of the probability density function, and it solves the equation $(\ln f(y))' = 0$:

$$\text{mode}(y) = \exp(\mu - \sigma^2) \quad \text{Eq. 11}$$

Median is the point in the intermediate position when all data are listed in order from the minimum value to the maximum value, where the cumulative value is 0.5:

$$\text{median}(y) = \exp(\mu) \quad \text{Eq. 12}$$

Mean is the average value of the whole data:

$$\text{mean}(y) = \exp(\mu + \sigma^2/2) \quad \text{Eq. 13}$$

In addition, the standard deviation of this log-normal distribution is calculated by:

$$\sqrt{V} = \sqrt{\exp(2\mu + \sigma^2) \cdot (\exp(\sigma^2) - 1)} \quad \text{Eq. 14}$$

In terms of the grain size distribution, the most concerned characterized values are the arithmetic mean value and standard deviation. Since the grain size is inherently relative to grain area, the area fraction is considered as grain size distribution weight. Fig. 5 (a-d) give the log-normal distribution fitting and corresponding cumulated distribution functions (CDFs) plotting of both ferrite and martensite on RD-TD and RD-ND planes, respectively. Generally, the grain size area fraction distribution obeys the log-normal

distribution. Besides, it is noted that the RD-ND plane shows a slightly smaller average grain size than the RD-TD plane. Therefore, for the 3D RVE generation, the average grain size of the RD-TD and RD-ND planes (Fig. 5 (e, f)) are employed as grain size distribution inputs. The arithmetical mean values of the fitted parameters are listed in Table 1. The ferrite in the investigated DP1000 has the average equivalent grain size less than 2 μm while martensite grains are approximately only a quarter of the ferrite grains.

4.1.3 Grain shape distribution

Similar to the grain size distribution, the grain shape distribution is characterized as the statistical frequency of the grain shape factor, which can be presented by the aspect ratio (asp) of each dimension. If the grains are regarded as equivalent ellipsoids in a 3D Cartesian coordinate system, the grain shape could be simply described by the length ratio of the three ellipsoid coordinate axes, marked as a:b:c. Besides, these three coordinate axes can be unified with the material coordinate system, i.e. RD-TD-ND axes, for many steels experienced the rolling deformation. Hence, a:b:c=1:1:1 refers to equiaxed grains and a:b:c=1:0.1:0.1 represents that grains are extremely elongated along RD (Delannay et al., 2009). In the 2D EBSD measurement, the aspect ratio is defined as the length ratio of the minor axis to the major axis of the ellipse fit to the grain, resulting in its range from 0 to 1. Therefore, with the investigations on RD-TD and RD-ND planes, the aspect ratio of RD:TD and RD:ND can be calculated respectively. It can be noticed that the grain shape trends to hold the consistent distribution independent from the grain size. Hence, the number fraction is employed as the grain shape distribution weight. Two or multiple peaks are observed in the grain shape distribution as shown in Fig. 6, especially for martensite grains, which means a more homogeneous distribution in grain shape. Generally, the grain shape still conforms with the log-normal distribution based on Eq. 9-Eq. 14. Here, $y = \text{asp}$ and $x = \ln(\text{asp})$. The CDFs of calculated distribution functions and experimental data are also checked to further certify the fitting quality of the distributions. In contrast to grain size, only the arithmetical average aspect ratios mean(asp) of three directions are used for grain shape characterization in RVEs. For the investigated DP1000,

RD:TD:ND=1:0.48:0.47 for ferrite and RD:TD:ND=1:0.49:0.48 for martensite, which describes a slightly elongated grain shape along RD.

4.1.4 Texture and misorientation distribution

The orientation distribution function (ODF) is employed to describe grain orientation distribution, as shown in Fig. 7. Both ferrite and martensite in DP1000 present the typical bcc rolled textures. The most important texture components in ferrite are the γ -fiber component $\{111\}<112>$ and off- γ -fiber component $\sim\{554\}<225>$, while in martensite, the rotated-cube component $\{001\}<110>$ has higher intensity. The grain orientation distribution of both phases on RD-TD and RD-ND planes is similar to each other. In order to numerically describe the grain orientation distribution, the texture index is introduced as a texture characteristics parameter. It is used for a rough classification of ODF into sharp and weak ones, and defined as the integration of orientation density of an ODF $f(g)$ (Bachmann et al., 2010):

$$t = - \oint f(g)^2 dg \quad \text{Eq. 15}$$

In addition, the normalized quantitative difference Δ_{diff} between an interested ODF $f(g)$ and a reference ODF $f_{\text{ref}}(g)$ is defined as well to evaluate the error between two ODFs, which could be calculated (Xie et al., 2013):

$$\Delta_{\text{diff}} = \frac{\oint (f(g) - f_{\text{ref}}(g))^2 dg}{\oint f_{\text{ref}}(g)^2 dg} \quad \text{Eq. 16}$$

Regarding the grain misorientation distribution, normally, there are two different ways for the misorientation description. One is based on the misorientation between nearest neighboring grains (marked as neighboring), and another is based on the misorientation between randomly picked grain pairs (marked as random), as shown in Fig. 8. It can be observed that the misorientation of ferrite and martensite grains show a similar distribution shape on both RD-TD and RD-ND planes. The probability distribution for the randomly picked misorientation angles follows the “Mackenzie distribution” (Mackenzie, 1964), which meets a cut-off at 62.8° due to the cubic polycrystals structure (Warrington and Boon, 1975) and displays an approximate maximum between 40° and 50° in a relationship with the

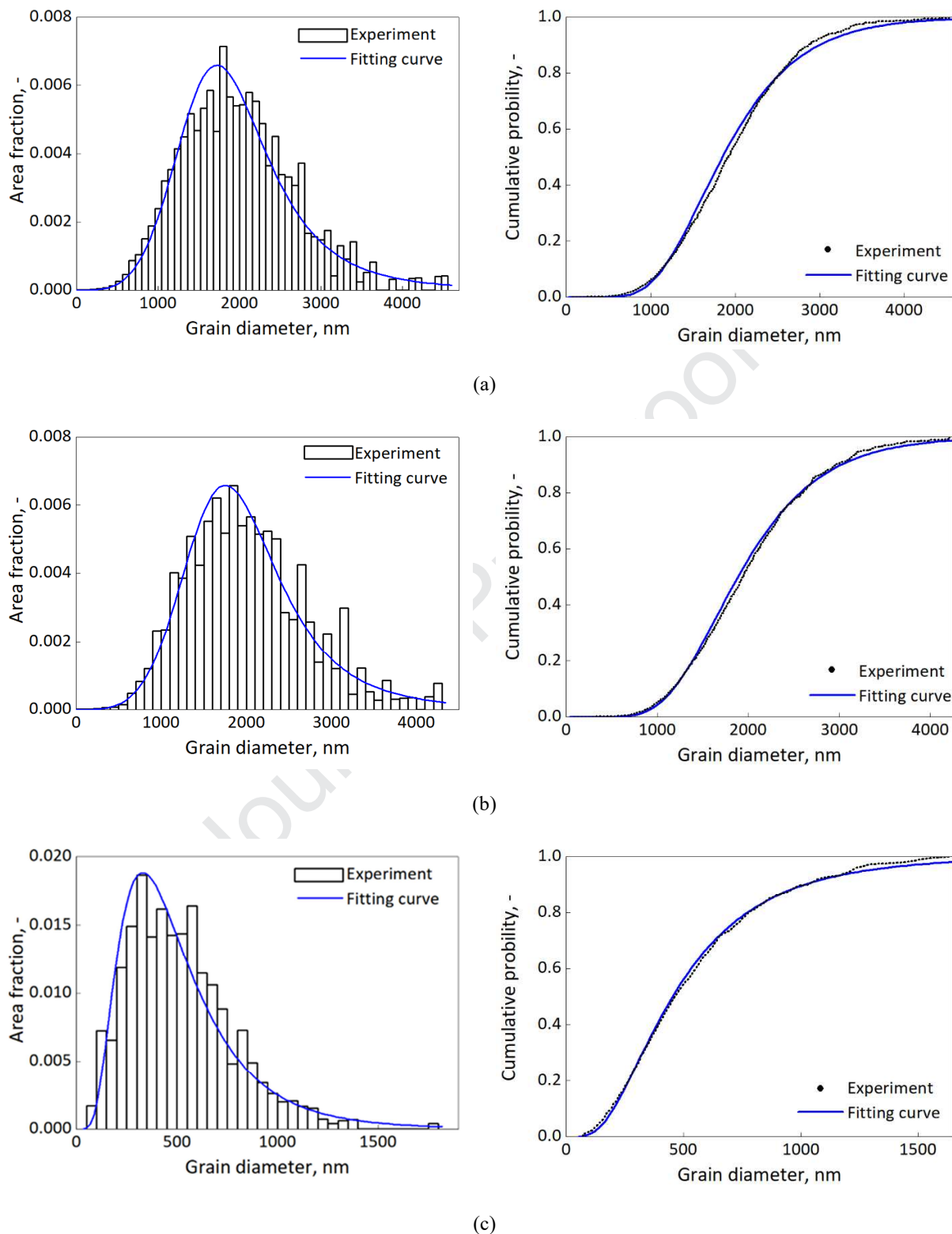
inherent material ODF. Meanwhile, the neighboring misorientation is more relative to the local morphology within the two phases. It has the same distribution range as the random misorientation distribution. While a peak fraction occurs at a slightly larger orientation range from 50° to 60°, revealing a larger grain boundary angles between neighboring grains. Besides, a distinctly secondary peak around 10°-15° on RD-TD planes indicates that the low angle grain boundaries (LAGBs) should not be negligible.

4.1.5 Remarks

To sum up, the microstructure characterization parameters can be determined for DP steel, as shown in Table 1. Generally, they are the phase fraction f , mean grain equivalent diameter d , mean grain shape factor asp , and texture index t for both phases. In detail, the expected value μ and standard deviation σ of grain size distribution, ODF figures of grain orientation distribution, and grain misorientation distribution figures are also characterized.

Table 1 Microstructure characterization of DP1000.

DP1000	Phase fraction, f	Average grain size, d (nm)	Grain size distribution, μ (nm)	Grain size distribution, σ (nm)	Average grain shape factor, asp	Texture index, t
Ferrite	0.55	1995.10	7.53	0.37	1:0.48:0.47	1.08
Martensite	0.45	536.01	6.11	0.59	1:0.49:0.48	1.05



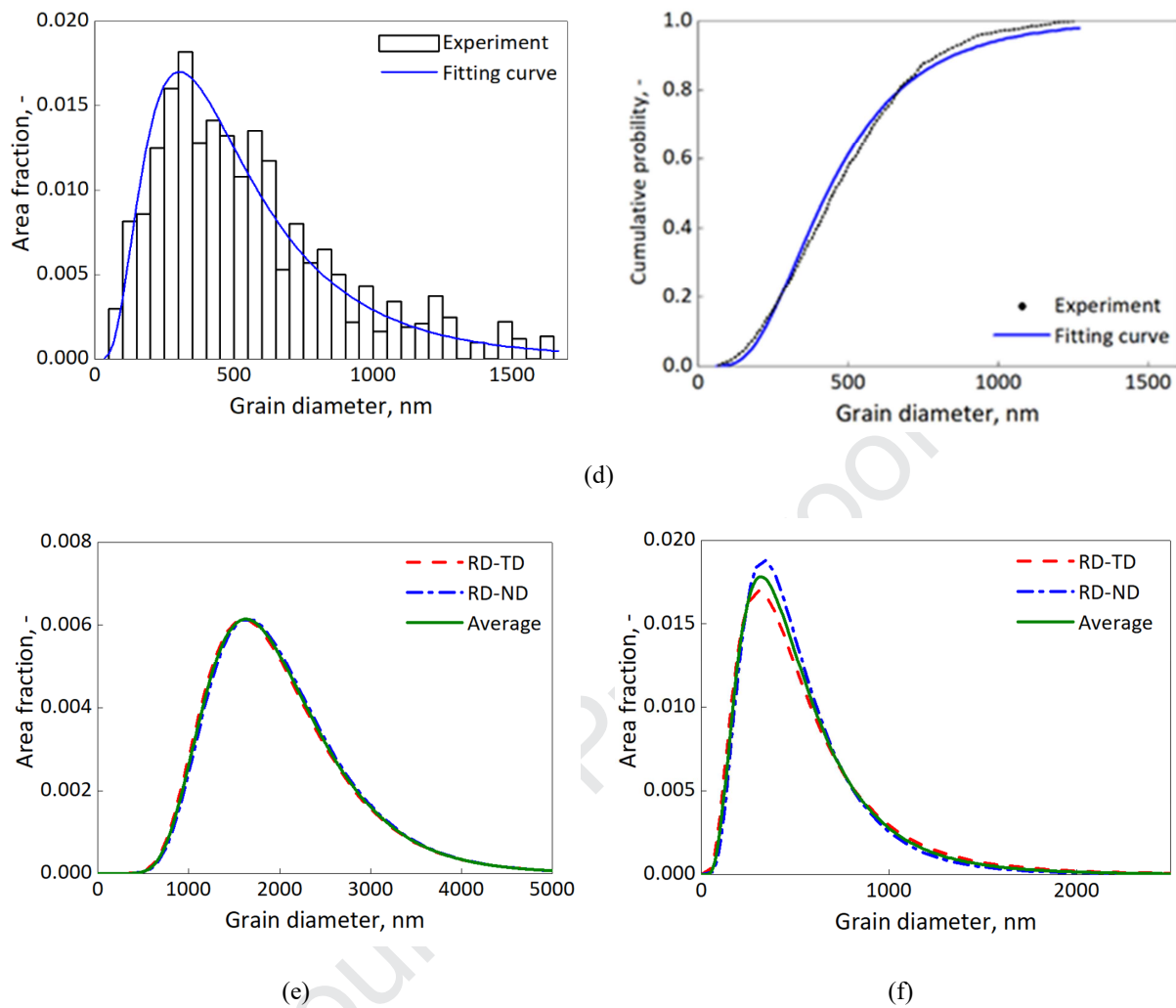
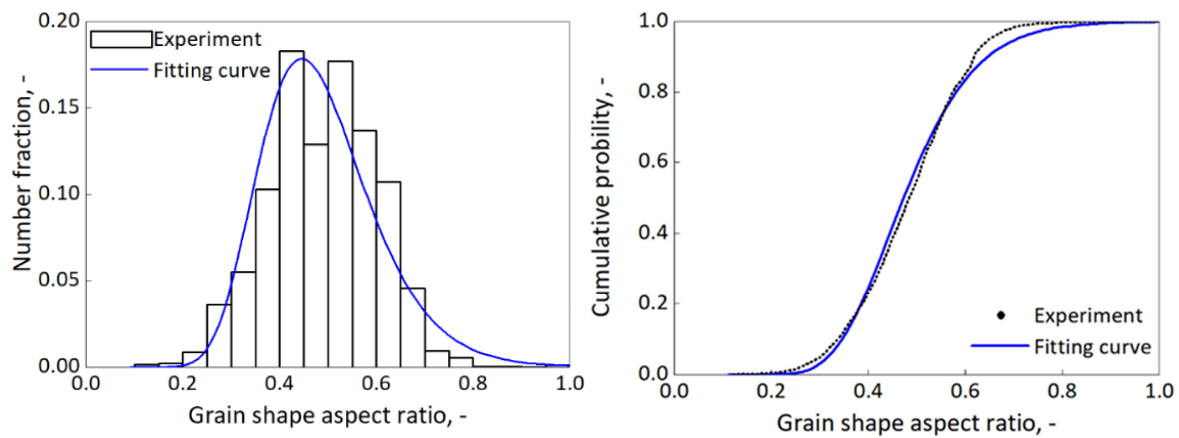
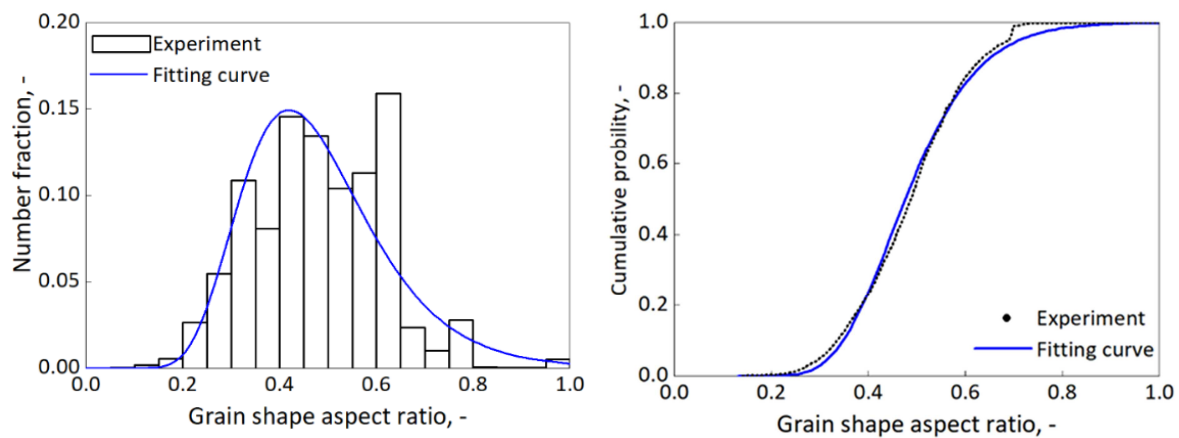


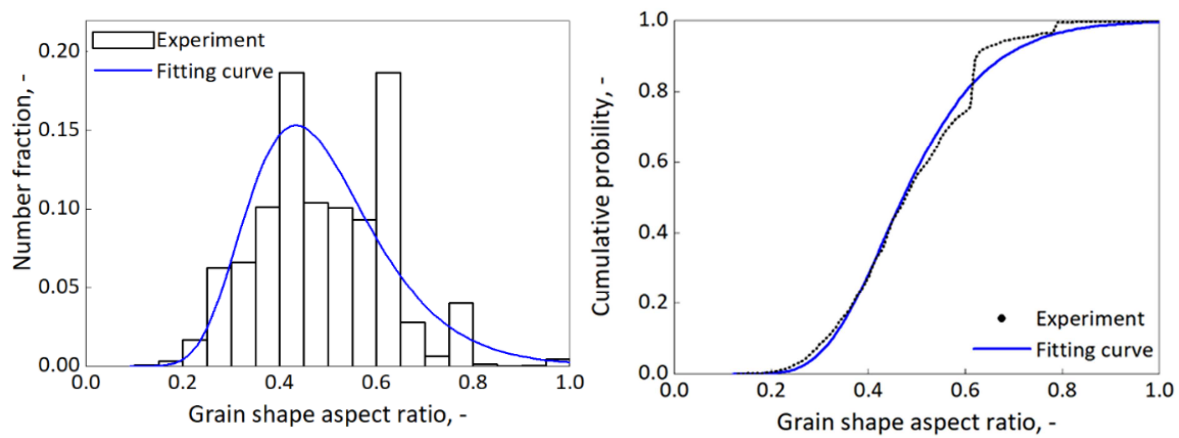
Fig. 5 Grain size log-normal distribution and cumulated distribution functions of DP1000 - (a) ferrite on RD-TD plane, (b) ferrite on RD-ND plane, (c) martensite on RD-TD plane, (d) martensite on RD-ND plane, (e) 3D average of ferrite phase, and (f) 3D average of martensite phase.



(a)



(b)



(c)

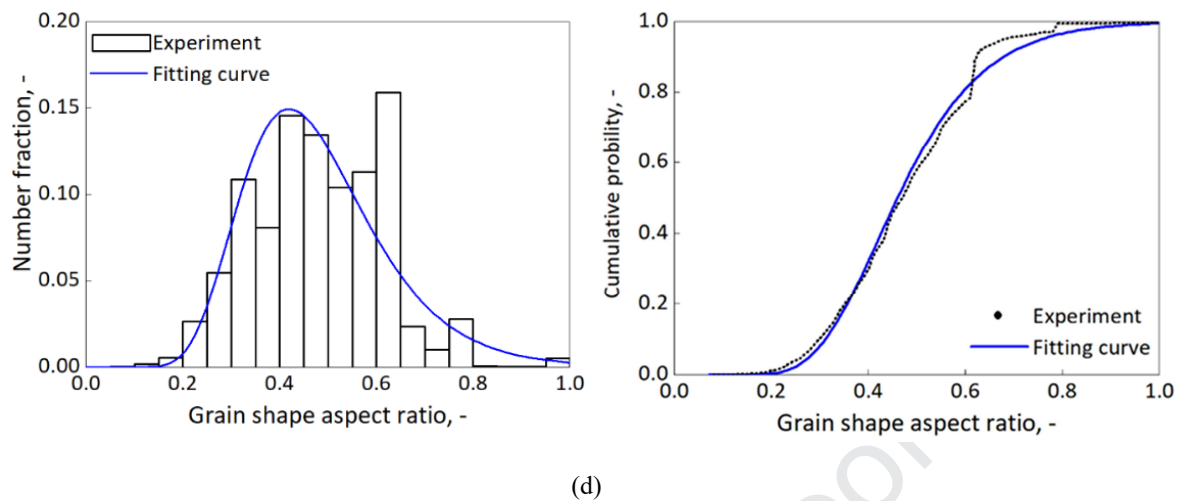


Fig. 6 Grain shape log-normal distribution and cumulated distribution functions of DP1000 - (a) ferrite phase on RD-TD plane, (b) ferrite phase on RD-ND plane, (c) martensite phase on RD-TD plane, and (d) martensite phase on RD-ND plane.

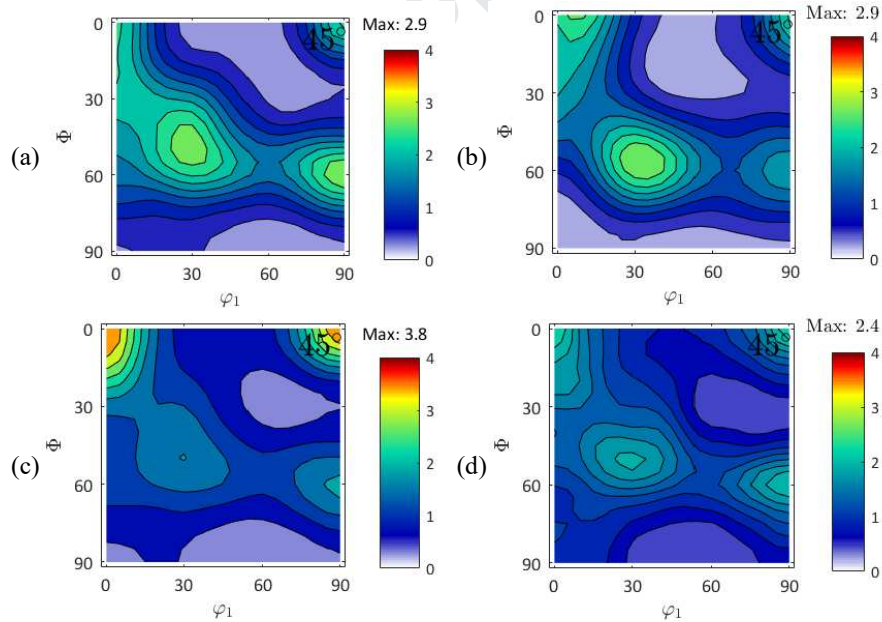


Fig. 7 Grain orientation distribution of DP1000 – ODF on $\phi_2=45^\circ$ section of (a) ferrite phase on RD-TD plane, (b) ferrite phase on RD-ND plane, (c) martensite phase on RD-TD plane, and (d) martensite phase on RD-ND plane.

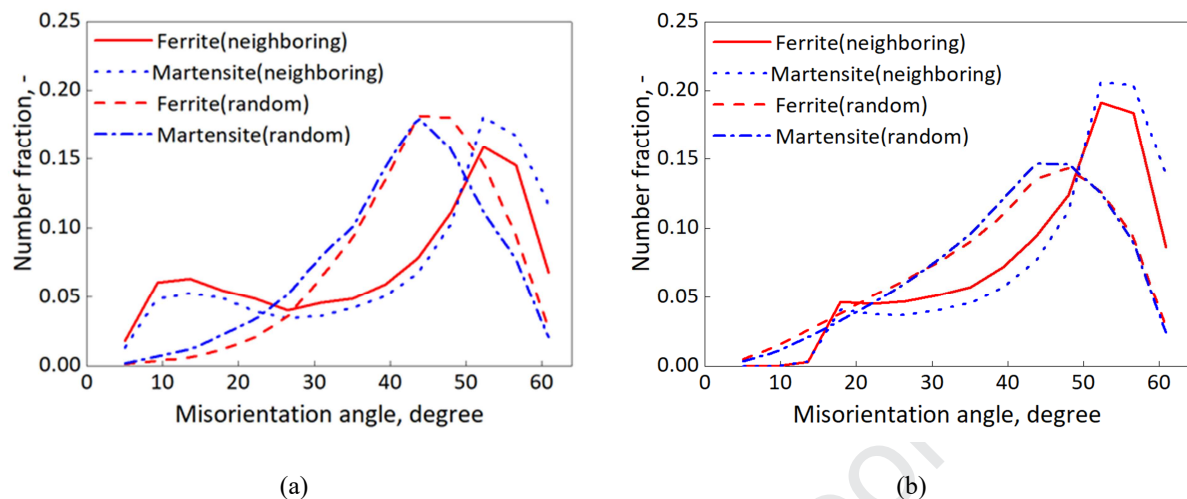


Fig. 8 Grain misorientation distribution of DP1000 on (a) RD-TD and (b) RD-ND planes.

4.2 Quantitative assessment criterion for the representativeness of microstructural features

With the characterized microstructure information of the investigated materials, Dream.3D (Groeber and Jackson, 2014) is used to generate the synthetic digital microstructure in the form of the representative volume. The software is one of very few RVE generation tools that give selective feedback on the quality of the RVEs generated, such as grain size, shape information. Although it also integrates an optimization approach to fit the experimental input while generating the RVEs, the derivation of the generated microstructure still exists and it is not quantified. In addition, the representativeness of RVE is also strongly affected by the numerical parameters, i.e. RVE size and mesh size. Hence, a microstructure representative assessment criterion (MRAC) based on the RVE generator output results is necessary to quantify the RVE quality and optimize the RVE numerical setting.

In terms of a fine-resolution RVE for a DP structure involving phase fraction, grain size, grain shape, grain orientation, etc., the comprehensive microstructural system already leads to the complex interactions between each individual feature. Hence, the assessment criterion should take into account not only each individual feature performance but also the overall quality to balance different microstructure aspects. For each single selected microstructural feature X , the absolute deviation ΔX between actual material input and RVE output can be calculated. Then the overall deviation Δ can be summarized as the average value of all

involved individual deviations. In terms of a DP structure, the basic focused individual microstructural features are the martensite phase fraction f , mean equivalent grain diameter d in grain size distribution function, mean grain shape factor asp in grain shape distribution function, and overall texture index t of grain orientation distribution function for each phase. Hence, seven parameters are analyzed in total. For the calculation of the individual deviation ΔX , a consistent function can be employed for phase fraction, mean equivalent grain diameter, mean grain shape factor, as well as the texture index:

$$\Delta X = \frac{|X_{\text{RVE}} - X_{\text{ref}}|}{X_{\text{ref}}} \times 100\% \quad \text{Eq. 17}$$

where the X_{ref} and X_{RVE} are the characterized values of the corresponding microstructural feature X from RVE input (i.e. material information based on EBSD in section 4.1) and output (i.e. microstructure information of RVE), respectively. It is noted that these seven parameters are recommended to be the basic microstructure features for assessment. More advanced features shall also be included for fine-tuning of the microstructure, which is shown in section 4.3. As one example, the overall deviation Δ can be formulated with the following basic microstructure features for DP1000:

$$\Delta = \text{mean}(|\Delta f_M|, |\Delta d_F|, |\Delta d_M|, |\Delta asp_F|, |\Delta asp_M|, |\Delta t_F|, |\Delta t_M|) \quad \text{Eq. 18}$$

The smaller the Δ value is, the better the RVE representativeness is. In addition, to visualize the general deviation, the microstructure representativeness assessment diagram (MRAD) as a radar chart is proposed. If the outline of the MRAD is assumed as the reference material information for X_{ref} and assigned to 1, The value X_r of the output RVE feature X_{RVE} on the radar diagram is:

$$X_r = X_{\text{ref}}/X_{\text{RVE}} \quad \text{Eq. 19}$$

With this criterion, the representativeness of RVE can be quantitatively assessed. It also should be noticed that the proposed criterion is helpful to evaluate the RVE representativeness on one hand, and on the other hand, it also assists to optimize the RVE with better representativeness, especially for the texture in RVE, as shown in section 4.3.

4.3 Algorithm for the optimization of the representative microstructure

The main use of the proposed method is in two folds:

- Minimize the generated scatter caused by RVE uncertainty;
- Optimize the RVE generation.

The first application of the method is rather straightforward. It is based on the fact that the basic RVE setup in terms of size and mesh is clear. During building up a 3D RVE based on the geometrical methods (Bargmann et al., 2018), no matter which algorithm is employed, e.g. the traditional Voronoi tessellation approaches or the recently developed statistically equivalent microstructures methods, the final solution of the so-called optimal germs or the best-fit ellipsoids could be non-unique. This leads to the fact for all the algorithms that even with the same numerical parameters setting, e.g. element number or mesh size, and the consistent material information input, the characteristics of the generated RVEs can be quite different, which is also the fundamental reason for the need of an evaluation criterion. For instance, with the material features in Table 1, Fig. 9 shows the MRAD of 10 generated RVEs with the same element number and mesh size setting. According to Eq. 19, the light grey outline of the MRAD is the input material information. It can be concluded that, with the statistically equivalent microstructures algorithm, the grain shape factor is well controlled for all RVEs with the identical numerical setting, while the phase fraction and grain size of the output RVE show about 10% deviation at largest and the texture index of ferrite could lead to a 35% difference from the input. This is caused by the randomly picking procedure of input Euler angles in RVE generation. With this specific numerical setting, RVE No. 7 presents the smallest overall deviation while RVE No. 2 shows the worst result. In Table 2, the individual microstructure features are also listed for these two RVEs.

For most of the studies involving RVEs, the setup of an optimal RVE actually starts with the RVE size and mesh size. In this study, by using the MRAC, the following two-step optimization procedure for the RVE generation is proposed:

- Optimization of the RVE numerical parameters based on the basic MRAC.
- Fine-tuning of the RVE microstructure features based on the advanced MRAC.

The basic MRAC in the context is refereeing to the seven microstructural features that have been chosen before and illustrated in Fig. 9. For the investigated DP1000, the performance of RVEs with variable

numerical settings are studied. Referring to a 3D cube RVE with voxel mesh, the numerical parameters including mesh size and element number in each dimension are focused. The entire RVE size is automatically decided by these two parameters.

This first numerical parameter to be decided is the mesh size. Considering the average grain size of ferrite and martensite, the mesh size in the range from 100 nm to 400 nm is studied as shown in Fig. 10. For all the RVEs, the total number of $40 \times 40 \times 40$ elements are fixed. It is noted that this is the element number, not the RVE size. The reason for using this parameter is that it can be directly correlated to the computational effort as shown in the second step. The MRAD shows that the shape factor for ferrite and martensite show a good response despite the mesh size. As analyzed in Table 1, the average grain size of ferrite is ~ 2000 nm and martensite is ~ 500 nm; hence, the mesh size changing from 400 nm to 200 nm gives similar output on ferrite grain size, while the smaller mesh size, 100 nm, provides better RVE performance on martensite grain size and phase fraction. However, with the identical element number, the smaller mesh size brings the smaller RVE size, i.e. less grain number and statistical information in RVE, which brings the distinct deviation on ferrite grain size in RVE with a mesh size smaller than 200 nm. This effect is also observed for the texture index, especially the one for ferrite. Consequently, a moderate mesh size should be chosen to balance the representativeness of martensite grain size and ferrite texture. Based on the overall deviation, Fig. 10 indicates 200 nm as the optimal mesh size of DP1000 RVE.

In terms of the element number in each dimension, both the individual and overall deviations in Fig. 11 demonstrate that the more elements in RVE result in better agreement with the input material microstructure owing to the increased RVE size with more grains. However, this is creating difficulty in the computational effort. With the von Mises benchmark simulations, the CPU hours of an RVE with 262,144 ($64 \times 64 \times 64$) elements is approximate 18 times more than an RVE with 64,000 ($40 \times 40 \times 40$) elements, while the overall representativeness deviation is only reduced by about 1%. Therefore, to balance the RVE representativeness and the model computational capacity, the element number of 40 in each dimension is chosen. To sum up, the optimal RVE numerical setting of the reference DP1000 is the mesh size of 200 nm and the element number of 40 in each dimension.

With the optimal structure, the RVE representativeness for each individual feature in the whole level can be satisfied. However, the overall agreement is not enough as the detailed microstructure distribution information should also be considered, especially for grain size and orientation. Therefore, the fine-tuning for RVE representativeness based on the advanced MRAC is necessary. For grain size, in addition to the mean value, the fine-tuning also includes the standard deviation of the distribution. That means the log-normal distribution, as well as the cumulated distribution of grain size from input and output of RVE, should be compared. For grain orientation, except for the texture index parameter for the general description of the spread of ODF, the overall error Δ_{diff} between input and output, ODFs should also be weighted according to Eq. 16. Furthermore, typical texture components, including the position and intensity of them, shall be further assessed. Based on the optimized RVE from the previous step, the grain size distributions match the actual material input pretty well in the whole grain size range for both phases according to Fig. 12. Comparing the ODF figures of martensite phase in optimal REV and EBSD measurement in Fig. 13 (a, b), the texture of martensite is accurately represented as well due to the larger martensite grain number - more than 1000 martensite grains in RVE, whereas the original RVE ferrite texture in Fig. 13 (d) cannot cover the main texture components in Fig. 13 (c), especially for the off- γ -fiber component $\sim\{554\}<225>$. This is mainly caused by the limited ferrite grain number and the default grain orientation assignment method in Dream.3D. Therefore, an additional post-process for grain orientation distribution optimization of the RVE is introduced.

The optimization is based on comparing the Euler angle of the most important texture components in reference material and original RVE output. In this specific case, this post-modified texture process is achieved by changing the Euler angles of the deviated grains in RVE to the Euler angle of typical texture component, $\{111\}<112>$. With this method, the optimal ferrite texture in Fig. 13 (e) shows a good agreement with the reference ODF. For the quantitative characterization of the improvement, the normalized quantitative difference Δ_{diff} , i.e. error between two ODFs, is calculated according to Eq. 16. The ODF difference Δ_{diff} between input and the original RVE is 0.49 while between input and the modified RVE is 0.36. Thus, texture optimization can be regarded as a success. Meanwhile, the random-

picked grain misorientation distribution is naturally captured with the well-represented RVE texture, especially for the martensite phase, as illustrated in Fig. 14. With respect to ferrite, although due to the limited ferrite grain number is optimal RVE, the misorientation distribution curve is waved, the similar tendency with input information is still captured. As shown in a recent paper (Biswas et al., 2019) on the misorientation effect, it has been pointed out with consistent grain orientation distribution, the grain-to-grain misorientation will not affect the stress-strain behavior in a notable way. They will have more impact on the strain localization and damage behavior of the material, which is beyond the scope of the current study.

The final optimal RVE is visualized in Fig. 15, which includes 51 ferrite grains and 1040 martensite grains in total. Table 3 displays the numerical setting and the output microstructural features of the optimal RVE compared with the actual material, illustrating that the reference material microstructure features are well represented in RVE generally. This optimal RVE can be employed for crystal plasticity parameter calibration in the following section.

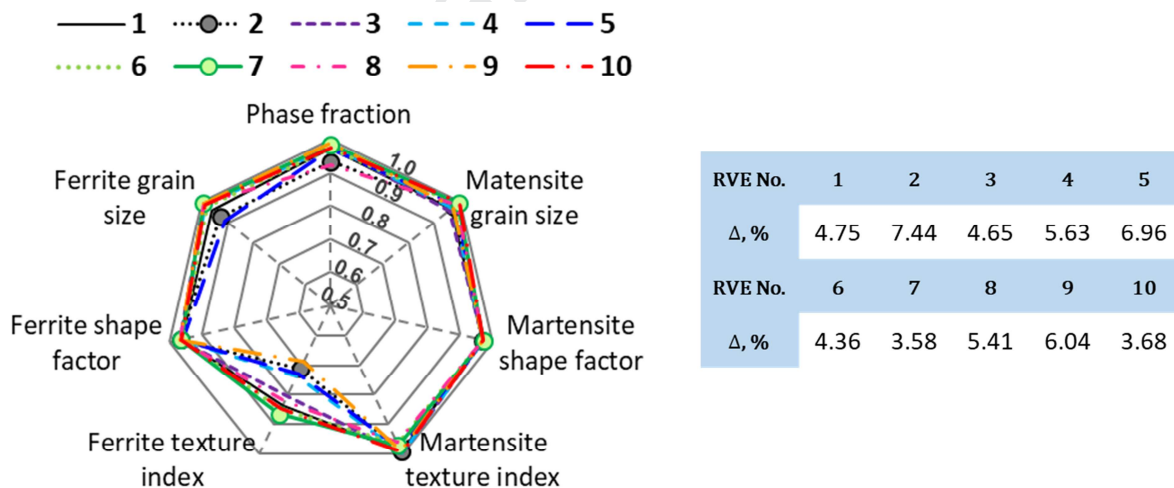


Fig. 9 Microstructure analysis of 10 RVEs with the same numerical parameter setting by MRAD.

Table 2 Microstructure features comparisons of RVEs with the same numerical parameter setting.

RVE No.	f_M	d_F , nm	d_M , nm	asp_F	asp_M	t_F	t_M	Δ , %
2	0.43	1843.65	568.86	1:0.49:0.46	1:0.51:0.47	1.52	1.06	7.44

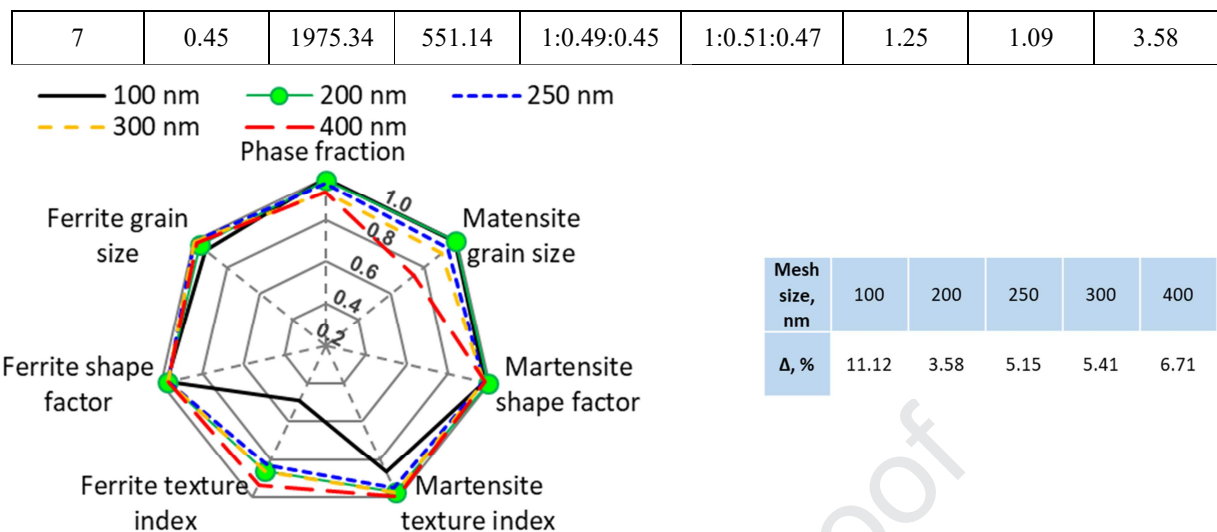


Fig. 10 Mesh size effect on the RVE representativeness.

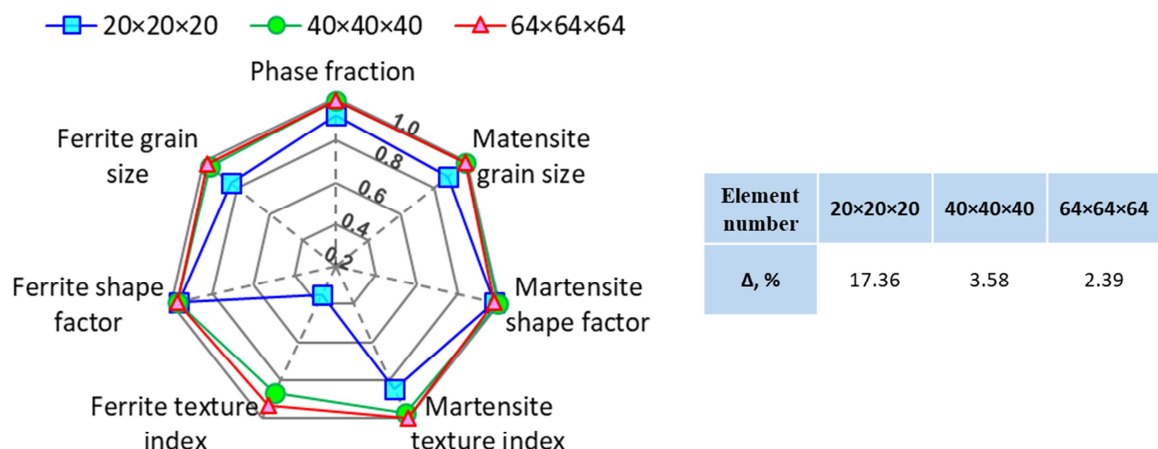


Fig. 11 Element number effect on the RVE representativeness.

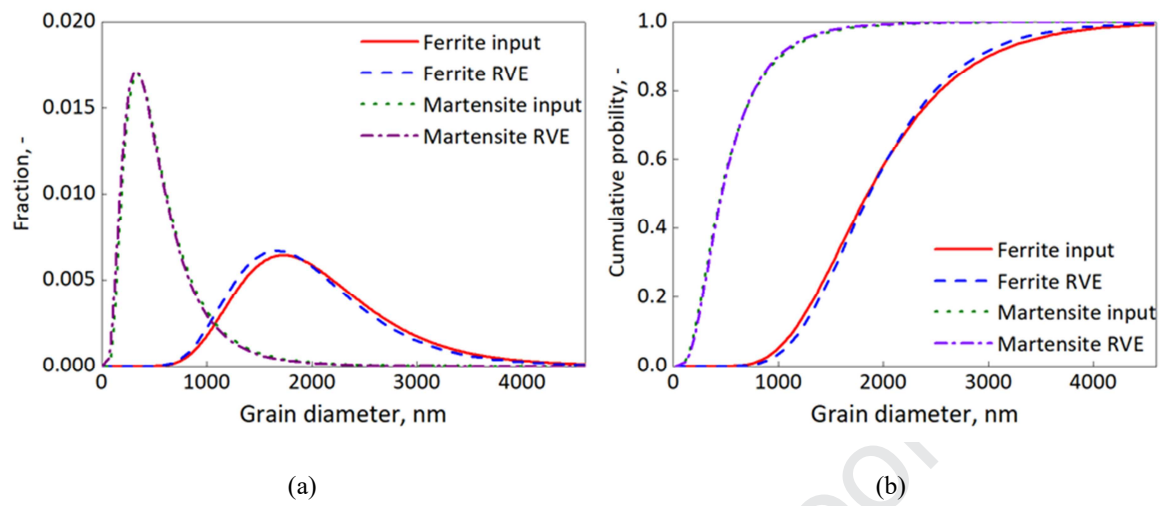


Fig. 12 The grain size distribution of the optimal DP1000 RVE.

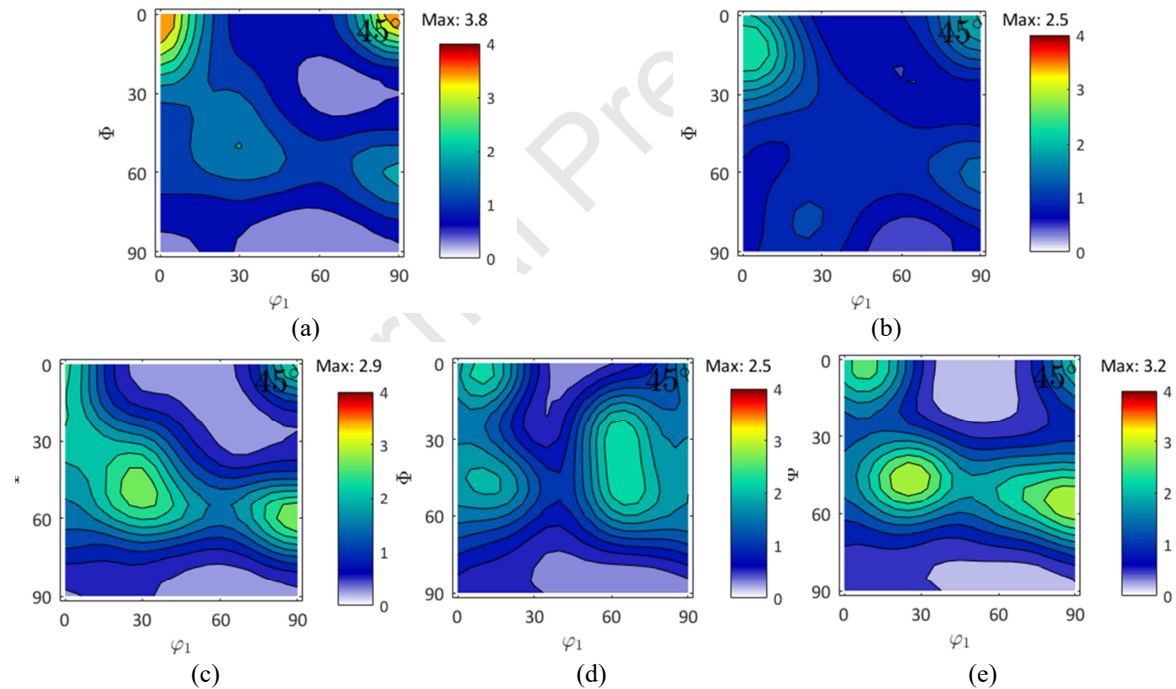


Fig. 13 Grain orientation distribution comparisons based on ODF with $\varphi_2=45^\circ$ section of: (a) EBSD measured martensite phase in DP1000 (b) martensite phase in the optimal DP1000 RVE, (c) EBSD measured ferrite phase in DP1000, (d) original ferrite phase in the DP1000 RVE, and (e) optimal ferrite texture in the optimal DP1000 RVE.

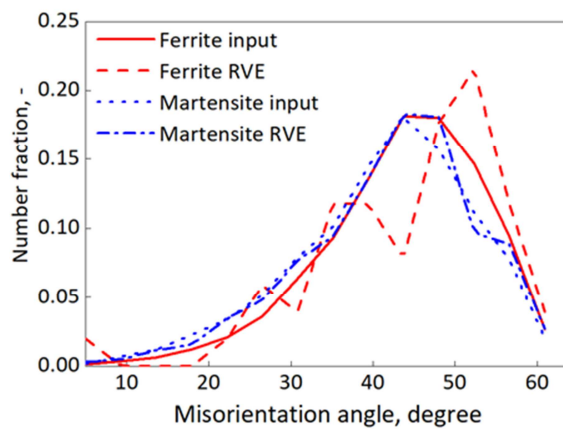


Fig. 14 Grain misorientation distribution of the optimal DP1000 RVE.

Table 3 Numerical setting and microstructure features of the optimal RVE of DP1000.

Mesh size, nm		RVE size, μm^3		Ferrite grain number		Martensite grain number	
200		8×8×8		51		1040	
	Phase fraction	Ferrite			Martensite		
		f	d, nm	asp	t	d, nm	asp
Input	0.45	1995.1	1:0.48:0.47	1.08	536	1:0.49:0.48	1.05
RVE	0.45	2033.4	1:0.49:0.45	1.25	578.4	1:0.51:0.47	1.09

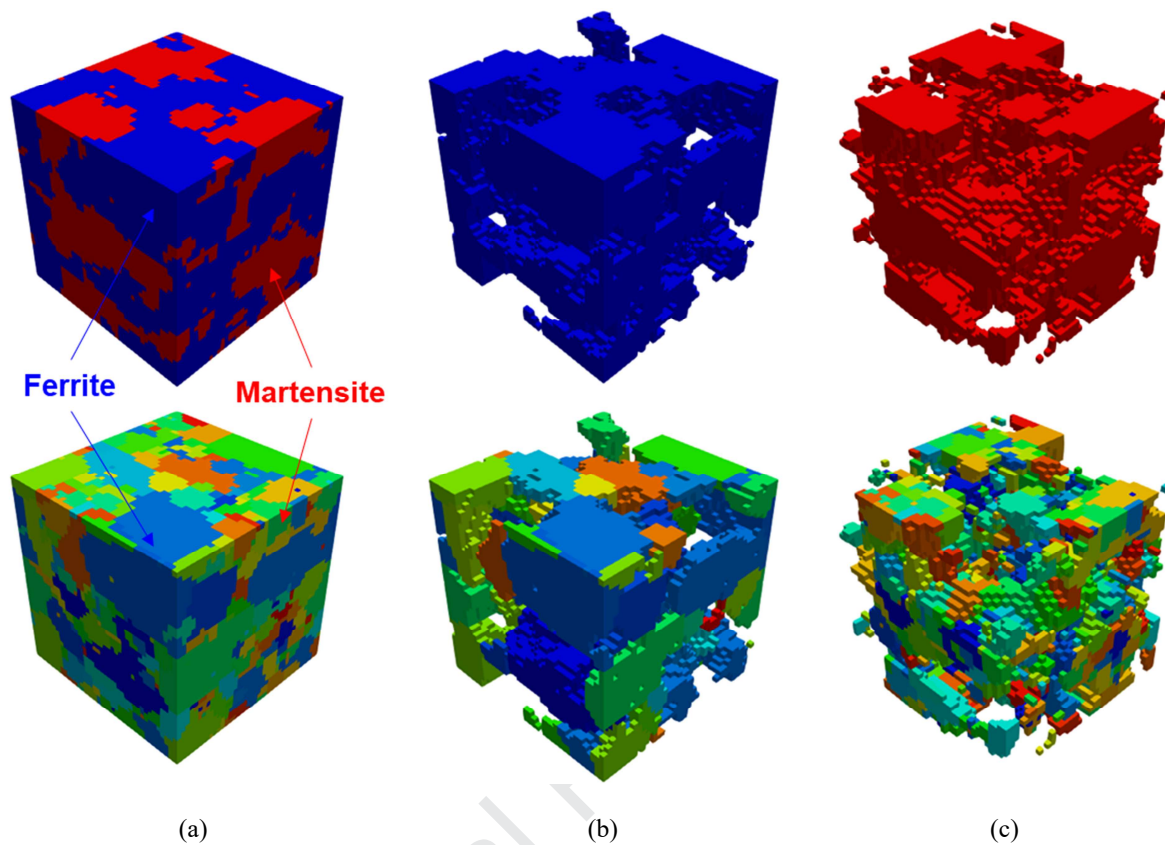


Fig. 15 Visualization of the optimal DP1000 RVE - (a) full structure, (b) ferrite phase, and (c) martensite phase (upper row for phase maps and lower row for grain maps).

5 Material parameter calibration of each individual phase

5.1 Strategy for the parameter calibration

Nanoindentation test is widely used to investigate the crystal plasticity deformation behavior and calibrate the crystal plasticity model parameters (Schmaling and Hartmaier, 2012; Wu et al., 2017). In terms of dual-phase steel, the nanoindentation test performed within a single grain area provides an opportunity to identify the micromechanical response of each phase. In the current study, this method is applied to the ferrite grains. However, with respect to the hierarchical martensite, the EBSD identified martensite grains by 5° misorientation are corresponding to the block level, which gives a characteristic grain size below the micro-level. This is very challenging for the current nanoindentation technique to gain reliable data. Owing to the ultra-fine martensite size, only one indent can be performed within one martensite island without confirmation on the repeatability. Most critically, large scatter is found for the nanoindentation test on martensite as the sub-structure boundary effects are present. Therefore, it is not recommended to use the nanoindentation test to calibrate the martensite CP behavior. Alternatively, an inverse method is introduced for the parameter calibration of DP1000. As illustrated in Fig. 16, there are two major steps to follow:

1. Calibrate the ferrite CP parameters based on the nanoindentation test and CPFEM modeling.
2. Inversely calibrate the martensite CP parameters based on the macroscopic DP1000 flow curve and ferrite CP parameters by means of the RVE based CPFFT modeling.

In the following sections, the experimental and corresponding modeling results will be introduced.

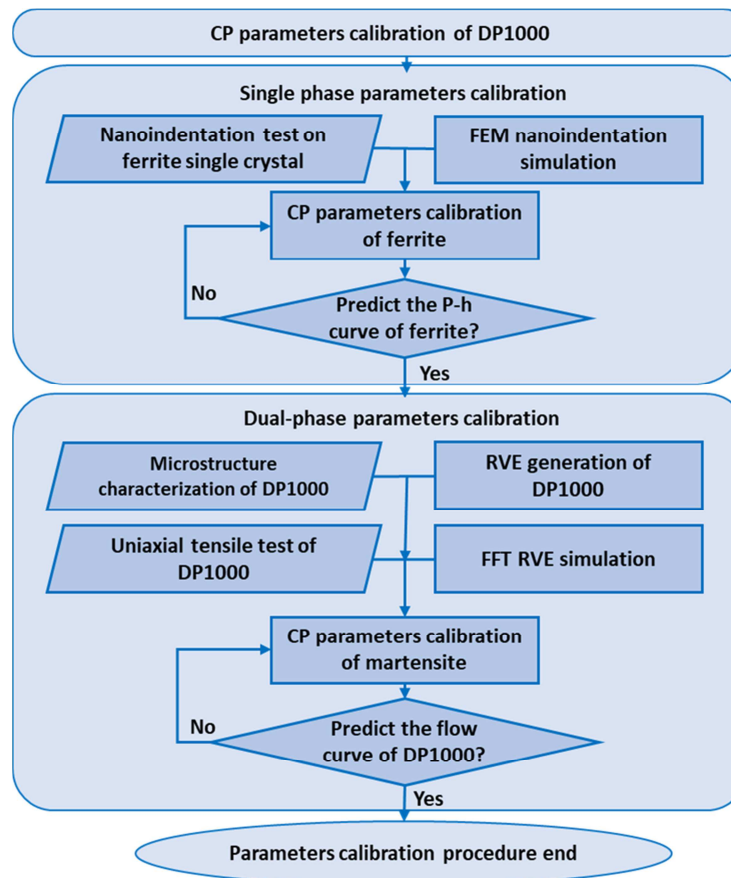


Fig. 16 Flow chart of crystal plasticity parameters calibration of DP1000.

5.2 Experimental results of nanoindentation and tensile tests

The nanoindentation experiments are performed by a TI980 TribolIndenter of Bruker Nano Surfaces Division in Aachen, Germany. For the investigated DP1000, due to the tiny grain size, the cube-corner indenter tip is chosen for the nanoindentation test on ferrite. It is the sharpest indenter resulting in the minimum affected area with the same indentation depth. With the shape of the cube-corner indenter, this tip has the sharpest total included angle of 90° and the highest aspect ratio of 1:1. With difference curvature radius from 40 nm to 100 nm, there will be different kinds of cube-corner tips, here, the curvature radius smaller than 40 nm is chosen.

In this study, scanning probe microscopy (SPM) is applied to locate the interesting area/grains coupling with the RD-TD EBSD orientations map in order to perform the indentation on the aimed spot. The displacement-controlled testing mode is chosen with a quasi-static loading rate, 0.1 nm/s. The indent depth

is controlled as 100 nm to avoid the possible influence from the other grains in the depth direction. For the applicability of crystal plasticity parameters, ferrite grains with different crystal orientations are chosen and multiple tests are performed on each grain. The SPM images after indentation are performed to validate the tests are performed on the intended grains and no microstructure boundaries are involved. For the detailed sample preparation and grain selections, the readers are referred to Wu et al. (2017).

Fig. 17 presents the nanoindentation set up on three different ferrite grains. The EBSD and SPM maps of the selected ferrite grains are shown in Fig. 17 (a)-(c) for Grain blue (B), purple (P), and green (G) with respect to their orientation colors on the inverse pole figure (IPF) color map, shown in Fig. 17 (d), respectively. It is clear that with these three relatively large grains, it is possible to conduct multiple parallel tests with enough distance between the indents. The load–displacement curves, i.e. P-h curves, will be employed for the CP parameter calibration of the ferrite phase, as shown in Fig. 19. For each crystal orientation, two parallel tests are shown as examples with black and red dot lines. It is noted the quantitative pile-up profile in 2D or 3D is not reliable to be used, as the scanning indenter for the profile is the same one used for indentation, which fails to give enough resolution for quantitative analysis.

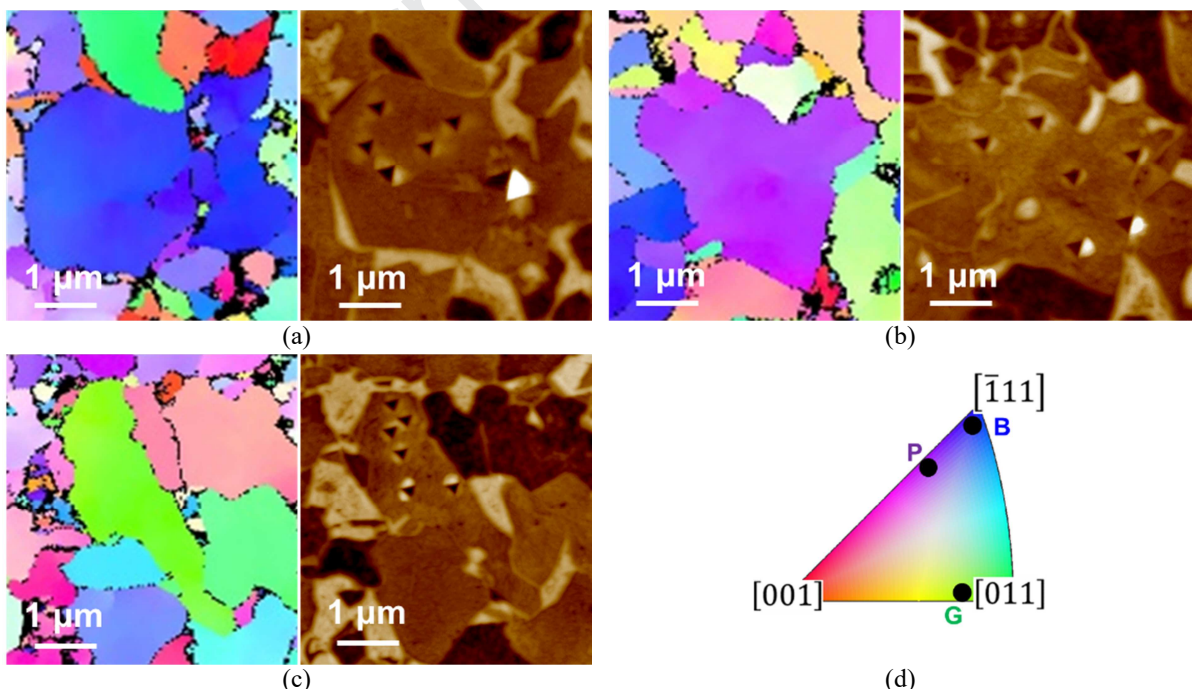


Fig. 17 Nanoindentation on ferrite grains with different orientations: (a-c) comparisons between EBSD and SPM images, (d) ND inverse pole figure for grain orientations.

The DP1000 flow curve along RD and TD is obtained by the uniaxial tensile test, in which the specimen of DP1000 is gripped at each end and stretched at quasi-static condition (strain rate of 0.0001 s^{-1}) and room temperature in a universal tensile test machine (Zwick 100kN). The sample geometry and testing procedure are reported in Lian et al. (2018) according to the European Standard EN 10002-1. The applied load and extension are measured by means of a load cell and strain gauge extensometer, respectively. The flow curve, hardening rate, Lankford coefficient of DP1000 can be analyzed with the uniaxial tensile test results and are displayed in Fig. 20 and Fig. 22. The RD stress-strain response is employed for the parameter calibration, while RD r-value evolution, as well as the TD stress-strain curve and r-value evolution, are used for the model and parameter validation.

5.3 CPFEM simulation of the nanoindentation test of the ferrite phase

By means of the CPFEM, the nanoindentation test can be simulated numerically and the CP parameters can be calibrated accordingly. In this study, the commercial finite element program Abaqus/Standard with a user-defined subroutine (UMAT) is used. Taking into account the actual cube-corner tip geometry employed in the test, the edge of the cube-corner is adjusted to be round as shown in Fig. 18 (a, b). This procedure also helps to improve the convergence of the simulation by avoiding the sharp edges. The 3D finite element model for single grain nanoindentation is shown in Fig. 18 (c). The grain dimension is $3\text{ }\mu\text{m} \times 3\text{ }\mu\text{m} \times 2\text{ }\mu\text{m}$. A fine mesh (finest as 30 nm) is set up in the contact area, which is the critical deformation area and a coarse mesh is applied for other regions. It is noted that the mesh on the cube corner tip zone is required to be coarser than the mesh in the contact area of the grain to avoid penetration. The element type is 3D solid elements with full integration (C3D8) in Abaqus. Frictionless conditions between the indenter and the specimen are assumed. The loading aptitude in the simulation is the same as that in the experiment.

In CPFEM, the crystal orientation is a required input from EBSD measurement. An iterative procedure is then run for the three grains to optimize the crystal plasticity parameters by minimizing the deviation of the predicted P-h curves from the experimental ones. Fig. 19 displays the simulated P-h curves (blue solid

lines) of the selected ferrite grains at 0.1 nm/s loading rate with the finally optimized parameters listed in Table 4. It is evident that the predicted P-h curves reach a reasonably good agreement with the experimental ones for all investigated ferrite grains. It is noted that the strain rate related parameters $\dot{\gamma}_0$ and m are not subjected to the optimization process. Instead, typical values from literature are applied as shown in Table 4 (Tasan et al., 2014).

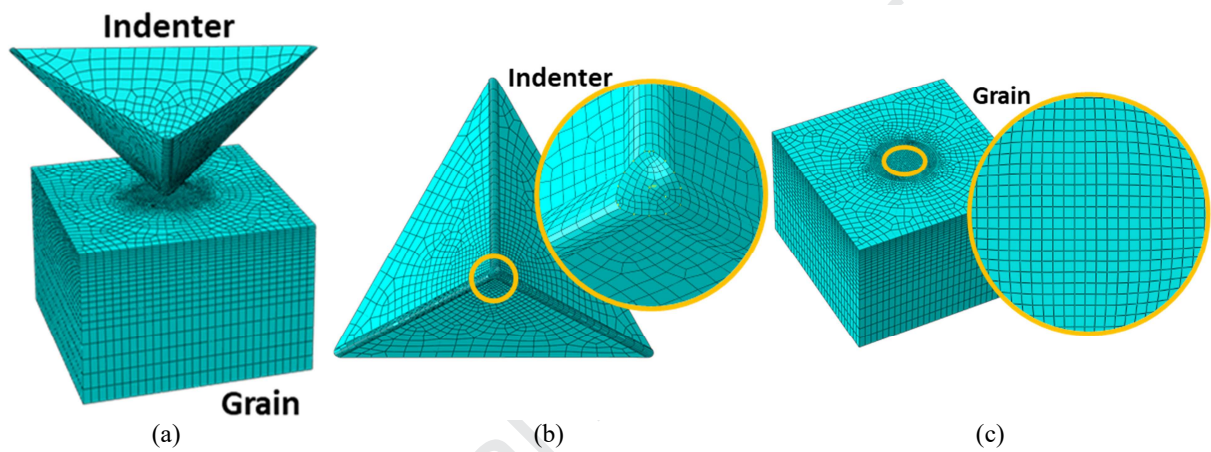


Fig. 18 Nanoindentation FE model: (a) 3D single grain nanoindentation FE model, (b) edge-rounded cube-corner indenter model, (c) single grain model.

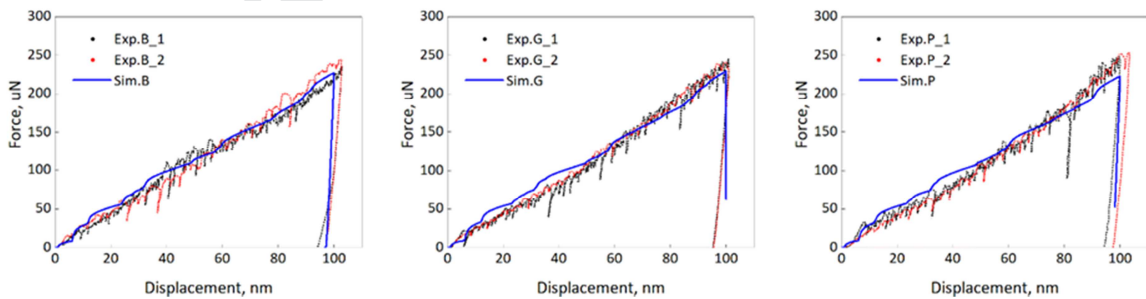


Fig. 19 Material parameters calibration by nanoindentation CPFEM simulation of ferrite grains in DP1000.

5.4 CPFFT simulation of the tensile test

The statistically-characterized microstructure-based RVE optimized in section 4.3 is employed as the sample of the DP steel to conduct the CP parameters calibration of martensite. As the optimal RVE composes 64,000 elements, considering the calculation performance limitation of FEM, the FFT spectral solver achieved by DAMASK (Roters et al., 2019) is employed to determine the solution for equilibrium and compatibility in finite strain formalism at each discrete material point. The calibration is based on the optimization of the stress-strain behavior along RD of the RVE as shown in Fig. 16. Finally, the calibrated quasi-static flow curve and corresponding hardening coefficient curve are shown in Fig. 20 (a,b) and the CP parameters of both ferrite and martensite phase in DP1000 and listed in Table 4. It is clear that a good agreement between the experiment and the RVE simulation is achieved. Combining Fig. 19 and Fig. 20, it can be concluded that this ferrite parameter set works well in both single-crystal nanoindentation and mesoscale RVE prediction.

To validate the RVE model as well as the calibrated CP parameters, the Lankford coefficient from the CPFFT simulation is compared with the experimental result and shown in Fig. 20 (c). In the experiments, a strong scatter is observed due to the measurement technique based on the 2D optical system. Considering the parallel tests, the model shows a very good prediction of the average initial r-value. In addition, the decreasing trend of the Lankford coefficient is also well captured by the simulation.

Furthermore, with the help of RVE virtual laboratory and calibration CP parameters, the grain-level local deformation behavior can be investigated. Combining the initial RVE phase map in Fig. 15 (a) and the local stress and strain patterns of DP1000 after uniaxial tension in Fig. 21, it is observed that in DP1000, martensite contributes to strength principally, while the plastic deformation is mainly occurring in the ferritic phase.

Besides, for further model and parameter validation, the uniaxial tensile test along TD is also performed and the numerical predictions on flow curve, hardening behavior, and r-value are compared with experimental results in Fig. 22. The stress-strain response and hardening behavior are well captured by the

micromechanics models. Similar to RD results, the r-value prediction is acceptable in the average level and the slightly decreased tendency is also observed in both numerical prediction and experiments.

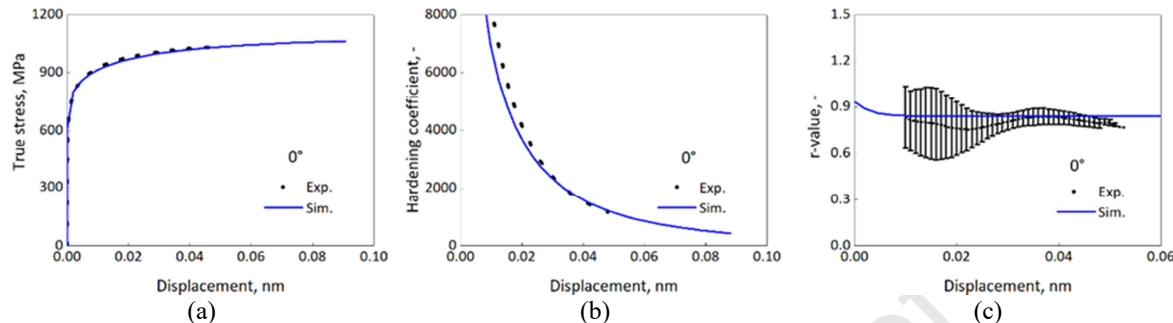


Fig. 20 RVE coupling crystal plasticity simulation of DP1000 uniaxial tensile tests along RD: (a) flow curves, (b) hardening coefficient curves, and (c) Lankford coefficient evolution curves.

Table 4 Crystal plasticity parameters of investigated DP1000.

Phase	τ_0 , MPa	τ_c^s , MPa	h_0 , MPa	a	$\dot{\gamma}_0$, s^{-1}	m
Ferrite	200	370	4500	1.3	0.001	0.05
Martensite	680	700	40000	2.5	0.001	0.05

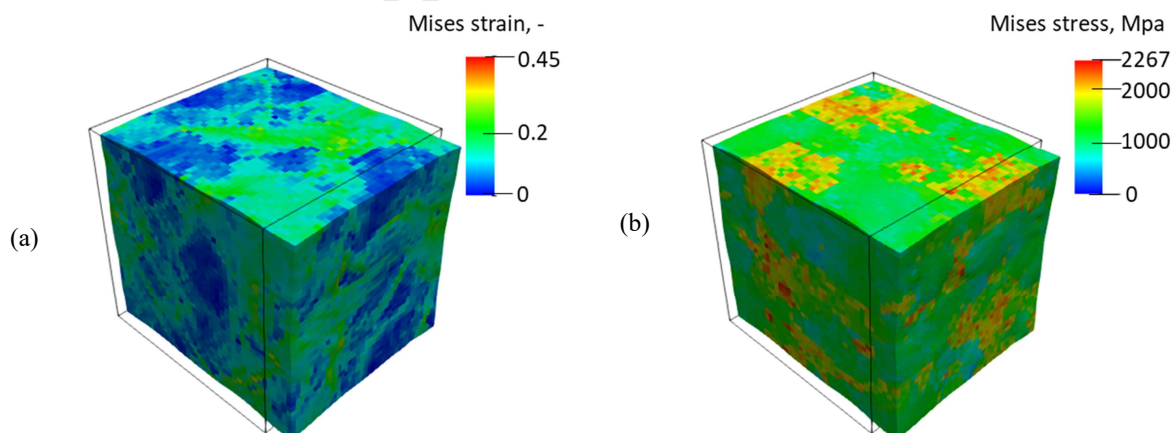


Fig. 21 Strain (a) and stress (b) patterns of DP1000 RD uniaxial tension simulation.

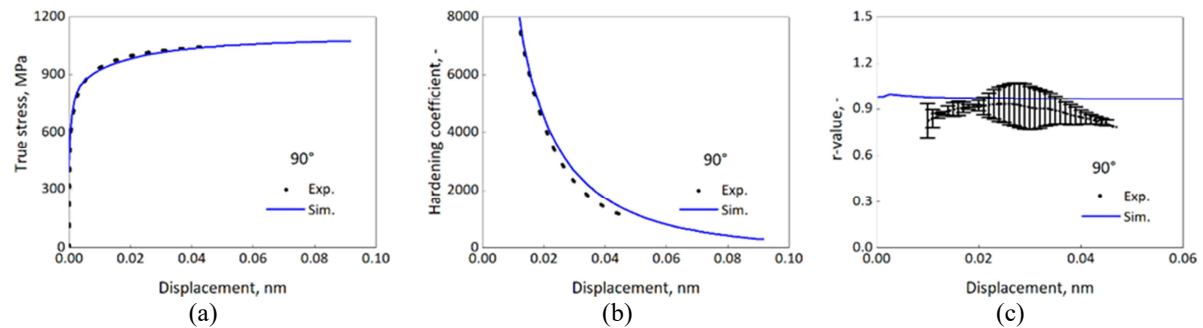


Fig. 22 RVE coupling crystal plasticity model prediction on DP1000 uniaxial tensile tests along TD: (a) flow curves, (b) hardening coefficient curves, and (c) Lankford coefficient evolution curves.

6 A sensitivity study of the microstructure effects on mechanical properties

With the approach coupling RVE generation and CP simulations, the bridge between macroscopic mechanical properties and microstructural features is built up. In this virtual laboratory, the RVE can be produced with variable microstructure and their corresponding plastic deformation behavior can be predicted by CP models. Consequently, the microstructure effects on mechanical properties can be investigated. For the interested mechanical property Y and microstructural feature X , the microstructure induced sensitivity S can be defined as the partial derivative of the output Y with respect to the input factor X (Sobol', 1990):

$$S = \frac{\partial Y}{\partial X} \text{ in } [X_{\min}, X_{\max}] \quad \text{Eq. 20}$$

In this way, the microstructural sensitivity is quantitatively analyzed. It should be noticed that the variable parameters for the sensitivity study are the specific RVE output factors rather than the input requirements. Therefore, the statistical characterization of the microstructure features in the output RVE should be carried out for the parameter sensitivity investigation. It is noted that for some microstructural features, the input factor cannot be represented by a single numeric value, the sensitivity definition according to Eq. 20 cannot be employed here. For example, the 3D grain shape factors are two aspect ratios from both TD/RD and ND/RD planes, even with the same input shape factor value for both phases and both planes, the generated RVE could perform a slight scatter on four output shape factor values. Besides, the texture component is normally indicated by Miller index or Euler angles, which needs at least three parameters. Hence, in order to analyze these features, the mechanical property Y_i is normalized with respect to the value Y_{Ref} gained from CP simulation of the optimal RVE for the reference material:

$$S_{\text{Nor}} = \frac{Y_i}{Y_{\text{Ref}}} \quad \text{Eq. 21}$$

Here, in terms of DP steel, the phase fraction, grain shape, and texture are considered. Regarding the mechanical behavior, strength property is quantitatively characterized by the predicted flow curves using the developed modeling strategy. In this study, the uniaxial tension along RD is focused, and three

indicators are chosen as the output Y for the microstructure parameter sensitivity on yielding and work hardening:

- Yielding point: σ_0 ;
- Flow stress at the true plastic strain equal to 0.05 (close to the uniform strain of the reference DP1000): $\sigma_{0.05}$;
- Arithmetical mean strain hardening rate n until the true plastic strain equal to 0.05: $n = \text{mean}(\frac{\partial\sigma}{\partial\varepsilon})$.

6.1 Phase fraction effect

The mechanical properties of DP steel are significantly influenced by the phase fraction of martensite and ferrite. RVEs with martensite volume fraction of 20%, 30%, 60%, and 70% are generated, as shown in Fig. 23. The numerical setting of RVEs keeps the same with the optimal one, i.e. with the element number of $40\times40\times40$ and the mesh size of $200\text{ nm}\times200\text{ nm}\times200\text{ nm}$. Additionally, with the use of MRAC and MRAD, the output of RVEs holds exactly the same distribution of grain size, shape, and orientation. This ensures also the comparison is only on the phase fraction without influences from other features. The detailed microstructure information is listed in Appendix A.1. The martensite phase fractions are also recalculated of the output RVEs, which show a good agreement with the input requirement. It is, however, noted that the crystal-level mechanical property might be dependent on the phase fraction due to the internal chemical composition partitioning, e.g. carbon. This effect is not taken into account for the current study.

Fig. 24 (a) illustrates the flow curves predicted by RVEs coupling CP with variable martensite phase fraction. The martensite phase fraction in the legend is marked based on the RVE input for readability. The accurate martensite phase fraction calculated from RVE output in Fig. 23 is considered for parameter sensitivity according to Eq. 20. It is demonstrated that with increasing phase fraction of martensite, the flow curve locates at a higher position, i.e., the strength of DP1000 increases with a higher phase fraction of martensite. This is determined by the CP parameter differences between ferrite and martensite in Table

4. The hierarchical substructure, enriched carbon content, higher dislocation density, and fine lath size contribute to the high strength and hardness of martensite. In addition, based on the quantitative sensitivity on σ_0 , $\sigma_{0.05}$, and n shown in Fig. 24 (b), changing of martensite phase fraction results in the slightly increased flow strength and distinctly decreased work hardening rate at the same time due to the lower strain hardening coefficient of martensite compared with ferrite. The yielding strength is more sensitive to the phase fraction in contrast.

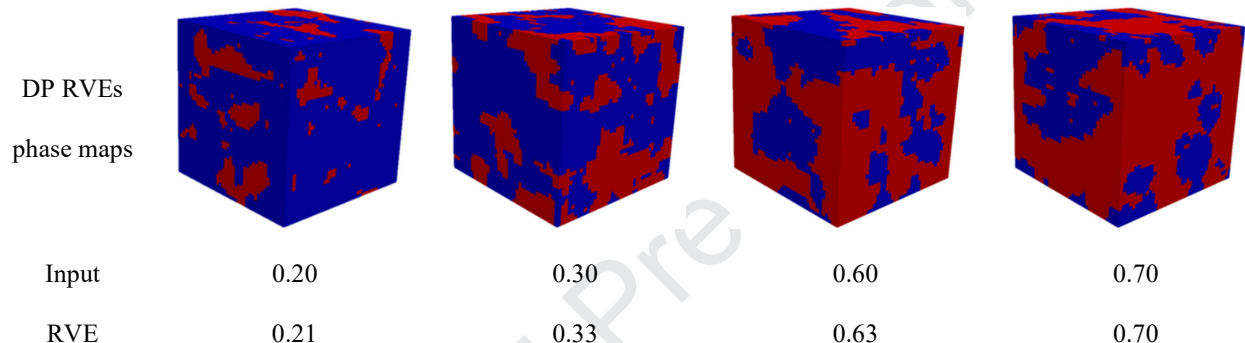


Fig. 23 RVEs with variable martensite phase fractions - phase maps (blue: ferrite and red: martensite).

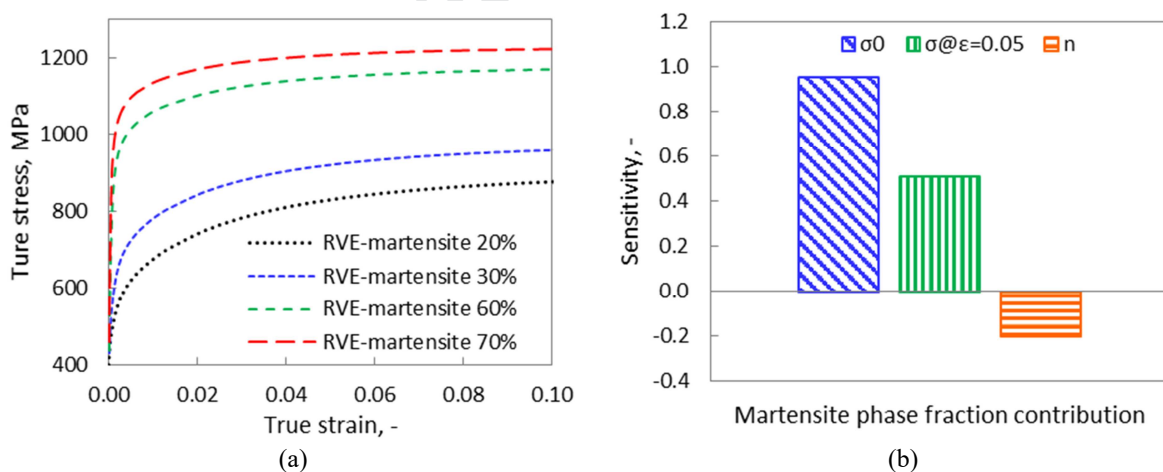


Fig. 24 Martensite phases fraction effect on the plastic flow behavior of DP steels: (a) predicted flow curves and (b) sensitivity parameters.

6.2 Grain shape effect

For the reference DP1000, the grain shape factor for ferrite and martensite is 1:0.49:0.48 and 1:0.49:0.49 respectively, indicating a moderately rolled microstructure. In order to study the effect of grain shape on plastic flow behavior, two extreme cases are considered: the grain shape aspect ratios are assumed as 1:1:1 for equiaxed grains in RD, TD, and ND and 1:0.1:0.1 for the drastically elongated grains along RD. In addition, two moderate cases are also taken into account to refine the shape effect study with 1:0.75:0.75 and 1:0.25:0.25. To minimize the variables, both phases are assigned with the same input shape factor. RVEs with different grain shapes are built, as shown in Fig. 25, including the analyzed shape aspect ratios. Once again, except for the desired shape aspect variation, the rest of the microstructural features are set the same as the reference material. Comparing the input and output features characterization (see Appendix A.2), even with the extremely elongated grains generation, the proposed MRAC and optimization procedure still manages to obtain the RVEs with statistics in a great agreement to the input data.

Fig. 26 demonstrates that grain shape has non-negligible influences on both the yielding point and strain hardening behavior. Due to the extremely high aspect ratio of 1:0.1:0.1, the distinct high strength from this RVE may be caused by the combined effects from both shape factor and boundary condition. But the decrease of grain shape aspect ratio from 1 to 0.25 also results in the increased yielding strength and decreased strain hardening rate, as shown in Fig. 26 (b). The decreased grain shape aspect ratio corresponds to the reduced grain shortest axis length in TD and ND, which results in the limited dislocation movement free path in these dimensions. In the range from 1:1:1 to 1:0.5:0.5, the investigated mechanical properties are closed to each other, but a weak tendency is still observed. In addition, the distorted grains also bring more heterogeneous microstructure morphology, which potentially leads to easier strain localization and damage.

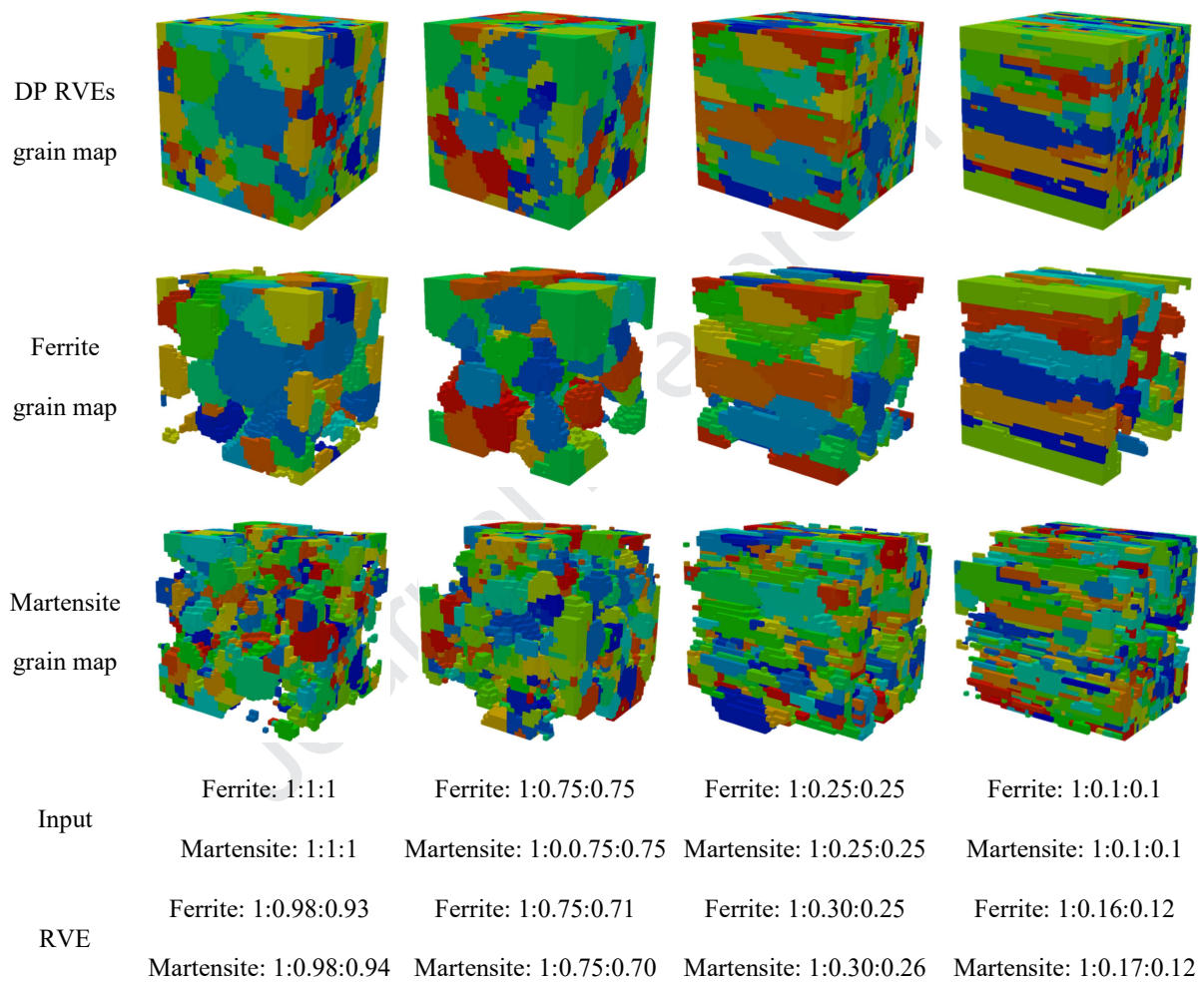


Fig. 25 RVEs with variable average grain shape factors - grain maps.

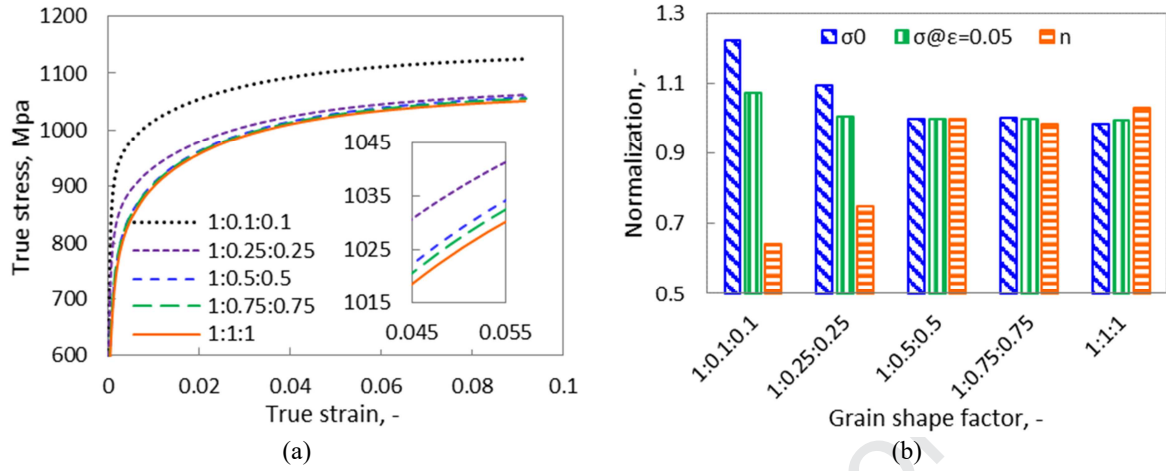


Fig. 26 Grain shape effect on the plastic flow behavior of DP steels: (a) predicted flow curves and (b) normalized sensitivity parameters.

6.3 Texture effect

Seven most important bcc texture components are considered, i.e. cube component $\{001\}<100>$, rotated cube component $\{001\}<110>$, Goss component $\{011\}<100>$, α -fiber component $\{112\}<110>$, γ -fiber components $\{111\}<110>$, $\{111\}<112>$, and off- γ -fiber component $\sim\{554\}<225>$, as shown in Fig. 27 (a). To simplify the analysis process and avoid the additional deviations introduced by variable phase fraction, grain size, and grain shape, the optimal RVE generated in section 4.3 is chosen. In addition, the texture for ferrite and martensite is also not distinguished to keep a single texture variable in the analysis. It is, however, noted that the crystal plasticity parameters for ferrite and martensite are different and kept the same as the reference DP1000 steel. There are 1091 grains in total, for every simulation, these grains are assigned with orientations differing the misorientation angular tolerance within 15° (refers to the larger angle grain boundary) from one special texture component center. An example ODF figure for the α -fiber component $\{112\}<110>$ on phi2 at 45° section is shown in Fig. 27 (b).

Fig. 28 (a) illustrates the flow curves predicted by RVE modeling. Analogously, the results for the yielding strength, flow strength at true plastic strain equal of 0.05, and the strain hardening rate are plotted in Fig. 28 (b). Generally, with the consistent CP parameter and RVE structure, the α -fiber component $\{112\}<110>$, γ -fiber components $\{111\}<110>$, $\{111\}<112>$ and off- γ -fiber component $\sim\{554\}<225>$ show a higher yield strength and tensile strength, whereas the cube $\{001\}<100>$, rotated cube

$\{001\}<110>$ and Goss $\{011\}<100>$ components show lower yield points and strain hardening rates. The latter observation matches the performance of martensite texture on work hardening at the macroscopic level. The most interesting texture is an α -fiber component $\{112\}<110>$, which performs the best strength behavior with not only the highest yielding point and tensile strength, but also the highest work hardening rate.

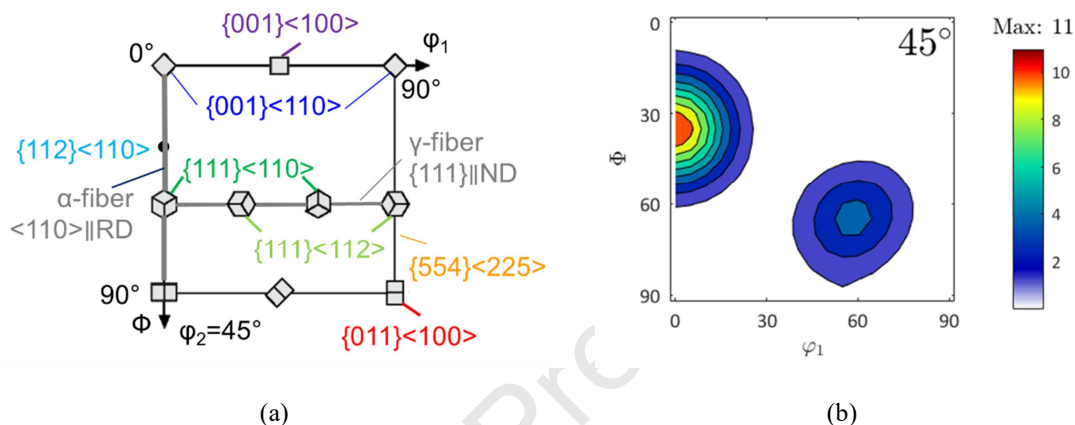


Fig. 27 (a) Schematic drawing of typical bcc texture components and (b) RVE texture with an α -fiber component $\{112\}<110>$ on ODF figure at $\phi_2=45^\circ$ section.

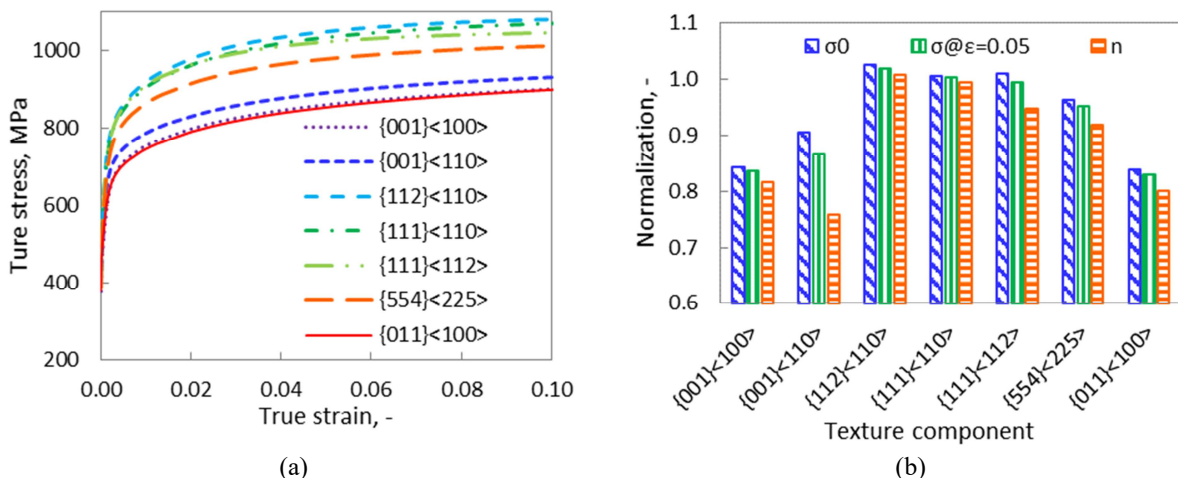


Fig. 28 Grain orientation effect on crystal plasticity: (a) predicted flow curves and (b) normalized sensitivity parameters.

6.4 Remarks

This section aims to demonstrate the applicability of the suggested strategy in the microstructure design field to optimize the mechanical properties. It offers a tool for variable yet accurate and quantitative analysis on the effect of each individual microstructure feature, as demonstrated above. It is not our intention to draw conclusive remarks at this stage to guide the microstructure design of DP steels, as there are still several important features missing. One of these is the effect of grain size. Due to the well-known Hall-Petch effect, grain size could contribute quite significantly to the plastic flow behavior. It is not included in the current study, as it requires a gradient sensitive crystal plasticity model, which is still under on-going development. We are incorporating a computational-light strain-gradient theory developed by Stephan Wulfinghoff et al. (Wulfinghoff et al., 2013; Wulfinghoff and Böhlke, 2012), which would give a chance to import the size effect into the simulation. Besides, except for the global response on stress-strain behavior, the local deformation representation shall also be considered in the future, as it would be critical for damage and failure analysis. Another aspect, which was also simplified here, is the assessment criterion for the mechanical properties. For a comprehensive analysis, it is necessary also to incorporate the anisotropic behavior of the microstructure in terms of both strength and plastic deformation as well as the damage behavior in damage-tolerant related design.

7 Conclusions

- A detailed method for the statistical and quantitative characterization of dual-phase steel (DP1000) with fine-grain microstructure is illustrated in terms of phase fraction, grain size, shape and orientation distribution of ferrite and martensite.
- A microstructure representativeness assessment criterion/diagram (MRAC/MRAD) is proposed based on the difference of the individual and global microstructural features between the synthetic structure and the experimental measurement. This strategy can be used to guide the evaluation of the representativeness of the synthetic microstructure for any microstructure generator.
- According to the proposed assessment method, a two-step optimization procedure is conducted to obtain the synthetic microstructure for the fine-grain structured DP1000. An additional fine-tuning procedure is considered for the representativeness in detailed microstructure distribution. The optimal synthetic microstructure is proven to be quantitatively representative for the real dual-phase material in terms of phase fraction, grain size and shape, and orientation distribution for each phase, especially for ferrite with only about 50 grains in the synthetic microstructure model.
- For the fine-grain DP steel, a parameter calibration procedure of the crystal plasticity model is proposed. Nanoindentation test with a cube-corner tip on the fine ferrite grains with an average grain diameter of 2 μm is used to calibrate the ferritic crystal plasticity parameters, while an inverse method is used for the martensitic crystal plasticity parameters by using the macroscopic tensile tests and modeling with the optimized synthetic microstructure model. A good agreement of the Lankford coefficient between the simulation and experiments validate the synthetic microstructure model and the calibrated parameters.
- With the proposed strategy, a microstructure sensitive analysis is performed on the plastic flow behavior of DP steels. Increasing the phase fraction and grain shape aspect ratio along the rolling direction increases the strength of DP steels. In addition, among seven bcc typical texture components, the α -fiber component $\{112\}<110>$ achieves high strength and work hardening rate.

Acknowledgments

The authors gratefully acknowledge the European Commission Research Fund for Coal and Steel (RFCS) [grant number: 709711] for the financial funding for the project. Dr. Ude Hangen from Bruker is acknowledged for providing the nanoindentation test support and valuable discussions. WL and JL are grateful to Wenwen Zhang and Yao Yao from IEHK for data processing, to Ilias Bellas from UTH for help on the nanoindentation simulation and to Dr. Alexander Schwedt from GFE for EBSD processing and related discussion. Simulations were performed with computing resources granted by RWTH Aachen University under project rwth0237.

Appendix

A.1 Microstructural features of RVEs with variable phase fractions.

		Phase fraction	Average grain size, nm	Average grain shape factor	Texture index
RVE1	Ferrite	0.79	1942	1:0.49:0.46	1.19
	Martensite	0.21	571	1:0.51:0.47	1.13
RVE2	Ferrite	0.67	1951	1:0.50:0.46	1.20
	Martensite	0.33	569	1:0.51:0.47	1.12
RVE3	Ferrite	0.37	1954	1:0.48:0.56	1.21
	Martensite	0.63	568	1:0.51:0.47	1.12
RVE4	Ferrite	0.30	1943	1:0.48:0.45	1.21
	Martensite	0.70	583	1:0.41:0.47	1.16

A.2 Microstructural features of RVEs with variable grain shape factors.

		Phase fraction	Average grain size, nm	Average grain shape factor	Texture index
RVE1	Ferrite	0.55	1967	1:0.98:0.93	1.24
	Martensite	0.45	561	1:0.98:0.94	1.11
RVE2	Ferrite	0.55	1926	1:0.75:0.71	1.25
	Martensite	0.45	568	1:0.75:0.70	1.08
RVE3	Ferrite	0.55	2000	1:0.30:0.25	1.22
	Martensite	0.45	561	1:0.30:0.26	1.05
RVE4	Ferrite	0.55	1975	1:0.16:0.12	1.21
	Martensite	0.45	556	1:0.17:0.12	1.10

References

- Akarapu, S., Zbib, H.M., Bahr, D.F., 2010. Analysis of heterogeneous deformation and dislocation dynamics in single crystal micropillars under compression. *International Journal of Plasticity* 26, 239-257.
- Arsenlis, A., M. Parks, D., Becker, R., V. Bulatov, V., 2004. On the evolution of crystallographic dislocation density in non-homogeneously deforming crystals. *Journal of the Mechanics and Physics of Solids* 52, 1213-1246.
- Arsenlis, A., Parks, D.M., 1999. Crystallographic aspects of geometrically-necessary and statistically-stored dislocation density. *Acta Materialia* 47, 1597-1611.
- Arsenlis, A., Parks, D.M., 2002. Modeling the evolution of crystallographic dislocation density in crystal plasticity. *Journal of the Mechanics and Physics of Solids* 50, 1979-2009.
- Asaro, R., Lubarda, V., 2006. Mechanics of Solids and Materials. Cambridge University Press, Cambridge.
- Avramovic-Cingara, G., Ososkov, Y., Jain, M.K., Wilkinson, D.S., 2009. Effect of martensite distribution on damage behaviour in DP600 dual phase steels. *Materials Science and Engineering: A* 516, 7-16.
- Bachmann, F., Hielscher, R., Schaeben, H., 2010. Texture Analysis with MTEX – Free and Open Source Software Toolbox. *Solid State Phenomena* 160, 63-68.
- Bag, A., Ray, K.K., Dwarakadasa, E.S., 1999. Influence of martensite content and morphology on tensile and impact properties of high-martensite dual-phase steels. *Metallurgical and Materials Transactions A* 30, 1193-1202.
- Bargmann, S., Klusemann, B., Markmann, J., Schnabel, J.E., Schneider, K., Soyarslan, C., Wilmers, J., 2018. Generation of 3D representative volume elements for heterogeneous materials: A review. *Progress in Materials Science* 96, 322-384.
- Becker, R., 1991. The effects of shear constraints on the lattice rotation of FCC crystals in (011) channel-die compression. *Journal of the Mechanics and Physics of Solids* 39, 459-476.
- Biswas, A., Prasad, M.R.G., Vajragupta, N., ul Hassan, H., Brenne, F., Niendorf, T., Hartmaier, A., 2019. Influence of Microstructural Features on the Strain Hardening Behavior of Additively Manufactured Metallic Components. *Advanced Engineering Materials* 21, 1900275.
- Bong, H.J., Lim, H., Lee, M.-G., Fullwood, D.T., Homer, E.R., Wagoner, R.H., 2017. An RVE procedure for micromechanical prediction of mechanical behavior of dual-phase steel. *Materials Science and Engineering: A* 695, 101-111.
- Calcagnotto, M., Adachi, Y., Ponge, D., Raabe, D., 2011. Deformation and fracture mechanisms in fine- and ultrafine-grained ferrite/martensite dual-phase steels and the effect of aging. *Acta Materialia* 59, 658-670.
- Choi, S.H., Kim, E.Y., Woo, W., Han, S.H., Kwak, J.H., 2013. The effect of crystallographic orientation on the micromechanical deformation and failure behaviors of DP980 steel during uniaxial tension. *International Journal of Plasticity* 45, 85-102.
- Delannay, L., Melchior, M.A., Signorelli, J.W., Remacle, J.F., Kuwabara, T., 2009. Influence of grain shape on the planar anisotropy of rolled steel sheets – evaluation of three models. *Computational Materials Science* 45, 739-743.
- Diehl, M., Groeber, M., Haase, C., Molodov, D.A., Roters, F., Raabe, D., 2017a. Identifying Structure–Property Relationships Through DREAM.3D Representative Volume Elements and DAMASK Crystal Plasticity Simulations: An Integrated Computational Materials Engineering Approach. *JOM* 69, 848-855.
- Diehl, M., Wicke, M., Shanthraj, P., Roters, F., Brueckner-Foit, A., Raabe, D., 2017b. Coupled Crystal Plasticity–Phase Field Fracture Simulation Study on Damage Evolution Around a Void: Pore Shape Versus Crystallographic Orientation. *JOM* 69, 872-878.
- Ebeling, T., Hartig, C., Laser, T., Bormann, R., 2009. Material law parameter determination of magnesium alloys. *Materials Science & Engineering A* 527, 272-280.
- Eisenlohr, P., Roters, F., 2008. Selecting a set of discrete orientations for accurate texture reconstruction. *Computational Materials Science* 42, 670-678.
- Fermi, E., Pasta, P., Ulam, S., Tsingou, M., 1955. Studies of the nonlinear problems, United States.
- Fivel, M., 2010. Discrete Dislocation Dynamics: Principles and Recent Applications, Multiscale Modeling of Heterogenous Materials. ISTE, pp. 17-36.

- Fonstein, N., 2017. 7 - Dual-phase steels, in: Rana, R., Singh, S.B. (Eds.), *Automotive Steels*. Woodhead Publishing, pp. 169-216.
- Ghosh, S., Shahba, A., Tu, X., Huskins, E.L., Schuster, B.E., 2016. Crystal plasticity FE modeling of Ti alloys for a range of strain-rates. Part II: Image-based model with experimental validation. *International Journal of Plasticity* 87, 69-85.
- Golovanenko, S.A., Fonstein, N.M., 1986. *Dual-Phase Low Alloyed Steels* [in Russian]. Metallurgiya, Moscow, Russia.
- Gottstein, G., 2004. *Physical Foundations of Materials Science*. Springer-Verlag Berlin Heidelberg, Berlin, Germany.
- Groeber, M.A., Jackson, M.A., 2014. DREAM.3D: A Digital Representation Environment for the Analysis of Microstructure in 3D. *Integrating Materials and Manufacturing Innovation* 3, 5.
- Gu, C., Lian, J., Bao, Y., Münstermann, S., 2019. Microstructure-based fatigue modelling with residual stresses: Prediction of the microcrack initiation around inclusions. *Materials Science and Engineering: A* 751, 133-141.
- Hama, T., Takuda, H., 2011. Crystal-plasticity finite-element analysis of inelastic behavior during unloading in a magnesium alloy sheet. *Int. J. Plasticity* 27, 1072-1092.
- Hielscher, R., Schaeben, H., 2008. A novel pole figure inversion method: specification of the MTEX algorithm. *Journal of Applied Crystallography* 41, 1024-1037.
- Hill, R., 1963. Elastic properties of reinforced solids: Some theoretical principles. *Journal of the Mechanics and Physics of Solids* 11, 357-372.
- Hill, R., 1966. Generalized constitutive relations for incremental deformation of metal crystals by multislip. *Journal of the Mechanics and Physics of Solids* 14, 95-102.
- Hill, R., Rice, J.R., 1972. Constitutive analysis of elastic-plastic crystals at arbitrary strain. *Journal of the Mechanics and Physics of Solids* 20, 401-413.
- Horvath, C.D., 2010. 2 - Advanced steels for lightweight automotive structures, in: Mallick, P.K. (Ed.), *Materials, Design and Manufacturing for Lightweight Vehicles*. Woodhead Publishing, pp. 35-78.
- Jiang, M., Devincre, B., Monnet, G., 2019. Effects of the grain size and shape on the flow stress: A dislocation dynamics study. *International Journal of Plasticity* 113, 111-124.
- Kadkhodapour, J., Schmauder, S., Raabe, D., Ziae-Rad, S., Weber, U., Calcagnotto, M., 2011. Experimental and numerical study on geometrically necessary dislocations and non-homogeneous mechanical properties of the ferrite phase in dual phase steels. *Acta Materialia* 59, 4387-4394.
- Kang, J., Ososkov, Y., Embury, J.D., Wilkinson, D.S., 2007. Digital image correlation studies for microscopic strain distribution and damage in dual phase steels. *Scripta Materialia* 56, 999-1002.
- Kim, D.-K., Kim, E.-Y., Han, J., Woo, W., Choi, S.-H., 2017. Effect of microstructural factors on void formation by ferrite/martensite interface decohesion in DP980 steel under uniaxial tension. *International Journal of Plasticity* 94, 3-23.
- Kraska, M., Doig, M., Tikhomirov, D., Raabe, D., Roters, F., 2009. Virtual material testing for stamping simulations based on polycrystal plasticity. *Computational Materials Science* 46, 383-392.
- Lai, Q., Brassart, L., Bouaziz, O., Gouné, M., Verdier, M., Parry, G., Perlade, A., Bréchet, Y., Pardoen, T., 2016. Influence of martensite volume fraction and hardness on the plastic behavior of dual-phase steels: Experiments and micromechanical modeling. *International Journal of Plasticity* 80, 187-203.
- Li, M., Sun, F., Li, D.F., O'Donoghue, P.E., Leen, S.B., O'Dowd, N.P., 2018. The effect of ferrite phases on the micromechanical response and crack initiation in the intercritical heat-affected zone of a welded 9Cr martensitic steel. *Fatigue & Fracture of Engineering Materials & Structures* 41, 1245-1259.
- Lian, J., Liu, W., Shen, F., Münstermann, S., 2017. Crystal plasticity assisted prediction on the yield locus evolution and forming limit curves. *AIP Conference Proceedings* 1896, 020030.
- Lian, J., Shen, F., Jia, X., Ahn, D.-C., Chae, D.-C., Münstermann, S., Bleck, W., 2018. An evolving non-associated Hill48 plasticity model accounting for anisotropic hardening and r-value evolution and its application to forming limit prediction. *Int. J. Solids Struct.* 151, 20-44.
- Lian, J., Yang, H., Vajragupta, N., Münstermann, S., Bleck, W., 2014. A method to quantitatively upscale the damage initiation of dual-phase steels under various stress states from microscale to macroscale. *Computational Materials Science* 94, 245-257.

- Liu, B., Raabe, D., Roters, F., Eisenlohr, P., Lebensohn, R.A., 2010. Comparison of finite element and fast Fourier transform crystal plasticity solvers for texture prediction. *Modelling and Simulation in Materials Science and Engineering* 18, 085005.
- Ma, A., Hartmaier, A., 2015. A study of deformation and phase transformation coupling for TRIP-assisted steels. *International Journal of Plasticity* 64, 40-55.
- Ma, A., Roters, F., Raabe, D., 2006a. A dislocation density based constitutive model for crystal plasticity FEM including geometrically necessary dislocations. *Acta Materialia* 54, 2169-2179.
- Ma, A., Roters, F., Raabe, D., 2006b. On the consideration of interactions between dislocations and grain boundaries in crystal plasticity finite element modeling – Theory, experiments, and simulations. *Acta Materialia* 54, 2181-2194.
- Ma, A., Roters, F., Raabe, D., 2006c. Studying the effect of grain boundaries in dislocation density based crystal-plasticity finite element simulations. *International Journal of Solids and Structures* 43, 7287-7303.
- Mackenzie, J.K., 1964. The distribution of rotation axes in a random aggregate of cubic crystals. *Acta Metallurgica* 12, 223-225.
- Madivala, M., Schwedt, A., Wong, S.L., Roters, F., Prahl, U., Bleck, W., 2018. Temperature dependent strain hardening and fracture behavior of TWIP steel. *International Journal of Plasticity* 104, 80-103.
- Mahnken, R., Schneidt, A., Antretter, T., Ehlenbröker, U., Wolff, M., 2015. Multi-scale modeling of bainitic phase transformation in multi-variant polycrystalline low alloy steels. *International Journal of Solids and Structures* 54, 156-171.
- Mainprice, D., Hielscher, R., Schaeben, H., 2011. Calculating anisotropic physical properties from texture data using the MTEX open-source package. *Geological Society, London, Special Publications* 360, 175.
- Mandal, S., Lao, J., Donegan, S., Rollett, A.D., 2018. Generation of statistically representative synthetic three-dimensional microstructures. *Scripta Materialia* 146, 128-132.
- McDowell, D.L., Dunne, F.P.E., 2010. Microstructure-sensitive computational modeling of fatigue crack formation. *International Journal of Fatigue* 32, 1521-1542.
- Nakamachi, E., Tam, N.N., Morimoto, H., 2007. Multi-scale finite element analyses of sheet metals by using SEM-EBSD measured crystallographic RVE models. *International Journal of Plasticity* 23, 450-489.
- Osipov, N., Gourgues-Lorenzon, A.F., Marini, B., Mounoury, V., Nguyen, F., Cailletaud, G., 2008. FE modelling of bainitic steels using crystal plasticity. *Philosophical Magazine* 88, 3757-3777.
- Pierman, A.P., Bouaziz, O., Pardoen, T., Jacques, P.J., Brassart, L., 2014. The influence of microstructure and composition on the plastic behaviour of dual-phase steels. *Acta Materialia* 73, 298-311.
- Prakash, A., Lebensohn, R.A., 2009. Simulation of micromechanical behavior of polycrystals: finite elements versus fast Fourier transforms. *Modelling and Simulation in Materials Science and Engineering* 17, 064010.
- Prasannavenkatesan, R., Przybyla, C.P., Salajegheh, N., McDowell, D.L., 2011. Simulated extreme value fatigue sensitivity to inclusions and pores in martensitic gear steels. *Engineering Fracture Mechanics* 78, 1140-1155.
- Prieto-Depedro, M., Martin-Bragado, I., Segurado, J., 2015. An atomistically informed kinetic Monte Carlo model of grain boundary motion coupled to shear deformation. *International Journal of Plasticity* 68, 98-110.
- Quey, R., Dawson, P.R., Barbe, F., 2011. Large-scale 3D random polycrystals for the finite element method: Generation, meshing and remeshing. *Computer Methods in Applied Mechanics and Engineering* 200, 1729-1745.
- Raabe, D., Roters, F., 2004. Using texture components in crystal plasticity finite element simulations. *International Journal of Plasticity* 20, 339-361.
- Raabe, D., Sachtleber, M., Zhao, Z., Roters, F., Zaeferer, S., 2001. Micromechanical and macromechanical effects in grain scale polycrystal plasticity experimentation and simulation. *Acta Materialia* 49, 3433-3441.
- Raabe, D., Zhao, Z., Mao, W., 2002a. On the dependence of in-grain subdivision and deformation texture of aluminum on grain interaction. *Acta Materialia* 50, 4379-4394.
- Raabe, D., Zhao, Z., Park, S.J., Roters, F., 2002b. Theory of orientation gradients in plastically strained crystals. *Acta Materialia* 50, 421-440.

- Ravi, S.K., Seefeldt, M., Van Bael, A., Gawad, J., Roose, D., 2019. Multi-scale material modelling to predict the material anisotropy of multi-phase steels. Computational Materials Science 160, 382-396.
- Rice, J.R., 1971. Inelastic constitutive relations for solids: An internal-variable theory and its application to metal plasticity. Journal of the Mechanics and Physics of Solids 19, 433-455.
- Roters, F., Diehl, M., Shanbhag, P., Eisenlohr, P., Reuber, C., Wong, S.L., Maiti, T., Ebrahimi, A., Hochrainer, T., Fabritius, H.O., Nikolov, S., Friák, M., Fujita, N., Grilli, N., Janssens, K.G.F., Jia, N., Kok, P.J.J., Ma, D., Meier, F., Werner, E., Stricker, M., Weygand, D., Raabe, D., 2019. DAMASK – The Düsseldorf Advanced Material Simulation Kit for modeling multi-physics crystal plasticity, thermal, and damage phenomena from the single crystal up to the component scale. Computational Materials Science 158, 420-478.
- Roters, F., Eisenlohr, P., Hantcherli, L., Tjahjanto, D.D., Bieler, T.R., Raabe, D., 2010. Overview of constitutive laws, kinematics, homogenization and multiscale methods in crystal plasticity finite-element modeling: Theory, experiments, applications. Acta Materialia 58, 1152-1211.
- Sanei, S.H.R., Fertig, R.S., 2015. Uncorrelated volume element for stochastic modeling of microstructures based on local fiber volume fraction variation. Composites Science and Technology 117, 191-198.
- Schmalung, B., Hartmaier, A., 2012. Determination of plastic material properties by analysis of residual imprint geometry of indentation. Journal of Materials Research 27, 2167-2177.
- Schmitz, G.J., Prahl, U., 2016. Handbook of Software Solutions for ICME. Wiley-VCH Verlag GmbH & Co. KGaA, Weinheim, Germany.
- Shen, H.P., Lei, T.C., Liu, J.Z., 1986. Microscopic deformation behaviour of martensitic–ferritic dual-phase steels. Materials Science and Technology 2, 28-33.
- Shinzato, S., Wakeda, M., Ogata, S., 2019. An atomistically informed kinetic Monte Carlo model for predicting solid solution strengthening of body-centered cubic alloys. International Journal of Plasticity.
- Sobol', I.M., 1990. On sensitivity estimation for nonlinear mathematical models [in Russian]. Matematicheskoe Modelirovaniye 2, 112-118.
- Soler, R., Molina-Aldareguia, J.M., Segurado, J., Llorca, J., Merino, R.I., Orera, V.M., 2012. Micropillar compression of LiF [111] single crystals: Effect of size, ion irradiation and misorientation. International Journal of Plasticity 36, 50-63.
- Tasan, C.C., Diehl, M., Yan, D., Bechtold, M., Roters, F., Schemmann, L., Zheng, C., Peranio, N., Ponge, D., Koyama, M., Tsuzaki, K., Raabe, D., 2015. An Overview of Dual-Phase Steels: Advances in Microstructure-Oriented Processing and Micromechanically Guided Design. Annual Review of Materials Research 45, 391-431.
- Tasan, C.C., Hoefnagels, J.P.M., Diehl, M., Yan, D., Roters, F., Raabe, D., 2014. Strain localization and damage in dual phase steels investigated by coupled in-situ deformation experiments and crystal plasticity simulations. International Journal of Plasticity 63, 198-210.
- Taylor, G.I., 1934a. The mechanism of plastic deformation of crystals. Part I.—Theoretical. Proceedings of the Royal Society of London. Series A, Containing Papers of a Mathematical and Physical Character 145, 362-387.
- Taylor, G.I., 1934b. The mechanism of plastic deformation of crystals. Part II.—Comparison with observations. Proceedings of the Royal Society of London. Series A, Containing Papers of a Mathematical and Physical Character 145, 388-404.
- Teferra, K., Graham-Brady, L., 2015. Tessellation growth models for polycrystalline microstructures. Computational Materials Science 102, 57-67.
- Uthaisangsuk, V., Münstermann, S., Prahl, U., Bleck, W., Schmitz, H.P., Pretorius, T., 2011. A study of microcrack formation in multiphase steel using representative volume element and damage mechanics. Computational Materials Science 50, 1225-1232.
- Vajragupta, N., Wechwanmanee, P., Lian, J., Sharaf, M., Münstermann, S., Ma, A., Hartmaier, A., Bleck, W., 2014. The modeling scheme to evaluate the influence of microstructure features on microcrack formation of DP-steel: The artificial microstructure model and its application to predict the strain hardening behavior. Computational Materials Science 94, 198-213.

- Van Houtte, P., Kanjarla, A.K., Van Bael, A., Seefeldt, M., Delannay, L., 2006. Multiscale modelling of the plastic anisotropy and deformation texture of polycrystalline materials. *Eur. J. Mech. A. Solids* 25, 634-648.
- Warrington, D.H., Boon, M., 1975. Ordered structures in random grain boundaries; some geometrical probabilities. *Acta Metallurgica* 23, 599-607.
- Woo, W., Em, V.T., Kim, E.Y., Han, S.H., Han, Y.S., Choi, S.H., 2012. Stress-strain relationship between ferrite and martensite in a dual-phase steel studied by in situ neutron diffraction and crystal plasticity theories. *Acta Materialia* 60, 6972-6981.
- Wu, B., Vajragupta, N., Lian, J., Hangen, U., Wechsuanmanee, P., Münstermann, S., 2017. Prediction of plasticity and damage initiation behaviour of C45E+N steel by micromechanical modelling. *Materials & Design* 121, 154-166.
- Wulfinghoff, S., Bayerschen, E., Böhlke, T., 2013. A gradient plasticity grain boundary yield theory. *International Journal of Plasticity* 51, 33-46.
- Wulfinghoff, S., Böhlke, T., 2012. Equivalent plastic strain gradient enhancement of single crystal plasticity: theory and numerics. *Proceedings of the Royal Society A: Mathematical, Physical and Engineering Sciences* 468, 2682-2703.
- Xie, Q., Gorti, S., Sidor, J.J., An, Y.G., Wang, Y.D., Lian, J., Lan, H., An, K., 2018a. Grain Orientation Dependence of the Residual Lattice Strain in a Cold Rolled Interstitial-Free Steel. *Steel Research International* 89.
- Xie, Q., Li, R., Wang, Y.D., Su, R., Lian, J., Ren, Y., Zheng, W., Zhou, X., Wang, Y., 2018b. The in-depth residual strain heterogeneities due to an indentation and a laser shock peening for Ti-6Al-4V titanium alloy. *Materials Science and Engineering: A* 714, 140-145.
- Xie, Q., Lian, J., Sun, F., Gan, B., Wang, Y., 2018c. The lattice strain ratio in characterizing the grain-to-grain interaction effect and its specific insight on the plastic deformation of polycrystalline materials. *The Journal of Strain Analysis for Engineering Design* 53, 353-363.
- Xie, Q., Van Bael, A., An, Y.G., Lian, J., Sidor, J.J., 2018d. Effects of the isotropic and anisotropic hardening within each grain on the evolution of the flow stress, the r-value and the deformation texture of tensile tests for AA6016 sheets. *Materials Science and Engineering: A* 721, 154-164.
- Xie, Q.G., Eyckens, P., Vegter, H., Moerman, J., van Bael, B., van Houtte, P., 2013. Polycrystalline Model Predictions of Flow Stress and Textural Hardening during Monotonic Deformation. *Key Engineering Materials* 554-557, 1157-1163.
- Xu, S., Guo, Y.F., Ngan, A.H.W., 2013. A molecular dynamics study on the orientation, size, and dislocation confinement effects on the plastic deformation of Al nanopillars. *International Journal of Plasticity* 43, 116-127.
- Yin, X., Chen, W., To, A., McVeigh, C., Liu, W.K., 2008. Statistical volume element method for predicting microstructure-constitutive property relations. *Computer Methods in Applied Mechanics and Engineering* 197, 3516-3529.
- Yu, C., Kang, G., Kan, Q., Zhu, Y., 2015. Rate-dependent cyclic deformation of super-elastic NiTi shape memory alloy: Thermo-mechanical coupled and physical mechanism-based constitutive model. *International Journal of Plasticity* 72, 60-90.
- Zambaldi, C., Yang, Y., Bieler, T.R., Raabe, D., 2012. Orientation informed nanoindentation of α -titanium: Indentation pileup in hexagonal metals deforming by prismatic slip. *Journal of Materials Research* 27, 356-367.
- Zhang, H., Diehl, M., Roters, F., Raabe, D., 2016. A virtual laboratory using high resolution crystal plasticity simulations to determine the initial yield surface for sheet metal forming operations. *International Journal of Plasticity* 80, 111-138.
- Zhang, K., Holmedal, B., Hopperstad, O.S., Dumoulin, S., Gawad, J., Van Bael, A., Van Houtte, P., 2015. Multi-level modelling of mechanical anisotropy of commercial pure aluminium plate: Crystal plasticity models, advanced yield functions and parameter identification. *International Journal of Plasticity* 66, 3-30.
- Zhao, Z., Mao, W., Roters, F., Raabe, D., 2004. A texture optimization study for minimum earing in aluminium by use of a texture component crystal plasticity finite element method. *Acta Materialia* 52, 1003-1012.

Zheng, Z., Waheed, S., Balint, D.S., Dunne, F.P.E., 2018. Slip transfer across phase boundaries in dual phase titanium alloys and the effect on strain rate sensitivity. International Journal of Plasticity 104, 23-38.

- A workflow for quantitatively characterizing the statistical microstructure of the fine-grained DP1000 is built up.
- A microstructure representativeness assessment criterion/diagram (MRAC/MRAD) is proposed to evaluate the representativeness of synthetic microstructure.
- An optimal synthetic microstructure model for the fine-structured DP1000 is established and validated.
- A crystal plasticity parameter calibration procedure for DP1000 is developed.
- The microstructural features effects are investigated via the virtual laboratory with the proposed strategy.

The authors declare no conflict of interests for the publication of this paper.